Journal of Sedimentary Research

Journal of Sedimentary Research, 2006, v. 76, 175–199
Research Article
DOI: 10.2110/jsr.2006.11

SEDIMENTOLOGICAL, PETROPHYSICAL, AND SEISMIC CHARACTERIZATION OF AN UPPER JURASSIC SHOREFACE-DOMINATED SHELF MARGIN (THE BOULONNAIS, NORTHERN FRANCE)

H. BRAAKSMA,[1] J.N. PROUST,[2] J.A.M. KENTER,[3] G.G. DRIJKONINGEN,[4] AND N. FILIPPIDOU[4]
[1]*Laboratoire de Tectonophysique-cc56, Université Montpellier 2, Place Eugène Bataillon, 34095 Montpellier, cedex 5, France*
[2]*UMR CNRS, 6118 Geosciences Rennes, Campus de Beaulieu, 35042 Rennes cedex, France*
[3]*Faculty of Earth and Life Sciences, Vrije Universiteit Amsterdam, The Netherlands*
[4]*Delft University of Technology, Delft, The Netherlands*
e-mail: Hendrik.Braaksma@dstu.univ-montp2.fr

ABSTRACT: **The integration of high-resolution (25 cm vertical spacing) and continuous quantitative data on grain size, carbonate content, porosity, density, and P-wave velocity from outcrop, borehole, and core (over 1000 samples) and a real seismic section allows a calibration of seismic sequence stratigraphic principles.**

This approach has been tested in the Boulonnais, along the English Channel coast in northern France on a succession of Upper Jurassic sharp-based shoreface deposits embedded in offshore marine shales.

Statistical analyses of grain-size distributions allow a characterization of hydrodynamic conditions and depositional processes affecting low-inclination shelf margins and create a framework for identifying locations of preferential and enhanced carbonate cementation, which exerts primary control on reservoir and acoustic properties.

Stratigraphic surfaces and systems tracts are quantified for physical properties and results in a quantitative mechanical sequence stratigraphic model. The combination of this model with seismic wavelets and a contrast between this synthetic and a real seismic section shows that key bounding sequence stratigraphic surfaces are in fact discontinuous reflectors.

Because stratal relationships of sharp-based shoreface deposits are subtle, physical contrasts are generally stratabound, and the deposits are typically not very thick, the geological recordings of sea-level falls and potential reservoirs are easily overlooked or go unseen in seismic sequence stratigraphic analyses. By defining key diagnostic seismic criteria for sharp-based shoreface deposits, this study contributes to the understanding of processes controlling sedimentary fills of epicontinental basins.

INTRODUCTION

The mechanisms controlling the temporal and spatial distribution of sediments and the physical properties of epicontinental basins are poorly understood because of the lack of modern analogues (Einsele 1985). Standard sequence stratigraphic models of sedimentary basins are based primarily on geometrical relationships of different sequences and systems tracts interpreted from seismic data (Vail et al. 1977). In energetic continental-shelf regimes and conventional continental margins, the accommodation space increases during progradation of sand bodies. The tendency is then to build up accretionary shorefaces with a relatively low average distance of progradation (Proust et al. 2001). However, when attempting to apply conventional sequence stratigraphic methodologies on low-inclination epicontinental basin fills that lack clear shelf–slope breaks, a much more flexible approach is needed (Taylor and Sellwood 2002). Because in these kinds of depositional settings few sediment gravity flows are generated and there is an overall tendency for sediments to aggrade and gravitate towards basin centers, geometrical relationships are very subtle.

Major components of epicontinental basin fills are sharp-based shoreface deposits. They are formed exclusively in these kinds of low-gradient depositional settings under forced regression and can prograde over relatively long distances (Posamentier et al. 1992). Because stratal relationships are subtle, physical contrasts generally are stratabound, and the deposits typically are not very thick, geological recordings of sea-level falls and potential reservoirs are easily overlooked or go unrecognized in seismic sequence stratigraphic analyses in these kinds of depositional settings. It is therefore essential to advance the understanding of first the quantitative relationship between geological parameters (e.g., grain size, carbonate content, and bioturbation) and their physical properties, and secondly the seismic response of sharp-based shoreface deposits.

This approach has been tested through a research project located in the Boulonnais, along the English Channel coast in northern France (Fig. 1). In the Boulonnais area, Upper Jurassic sharp-based shoreface deposits embedded in offshore marine shales are exposed in freshly weathered sea cliffs. Furthermore, fully cored (and logged) boreholes and seismic experiments (Proust et al. 2001; Mahieux et al. 1998) were drilled and acquired in and over exactly the same, but now subsurface water saturated, succession of sequences in the intertidal zone and offshore (Fig. 1B).

Numerical models provide insight into the formation and preservation of stratigraphic sequences (e.g., STRATAFORM, Syvitski and Hutton 2001; Syvitski and Bahr 2001; e.g., BARSIM, Storms et al. 1999; Storms et al. 2002; Storms and Swift 2003; e.g., STRATA, Flemings and Grotzinger 1996; e.g., CARBONATE 3-D, Warrlich et al. 2002). These

 1527-1404/06/076-175/$03.00

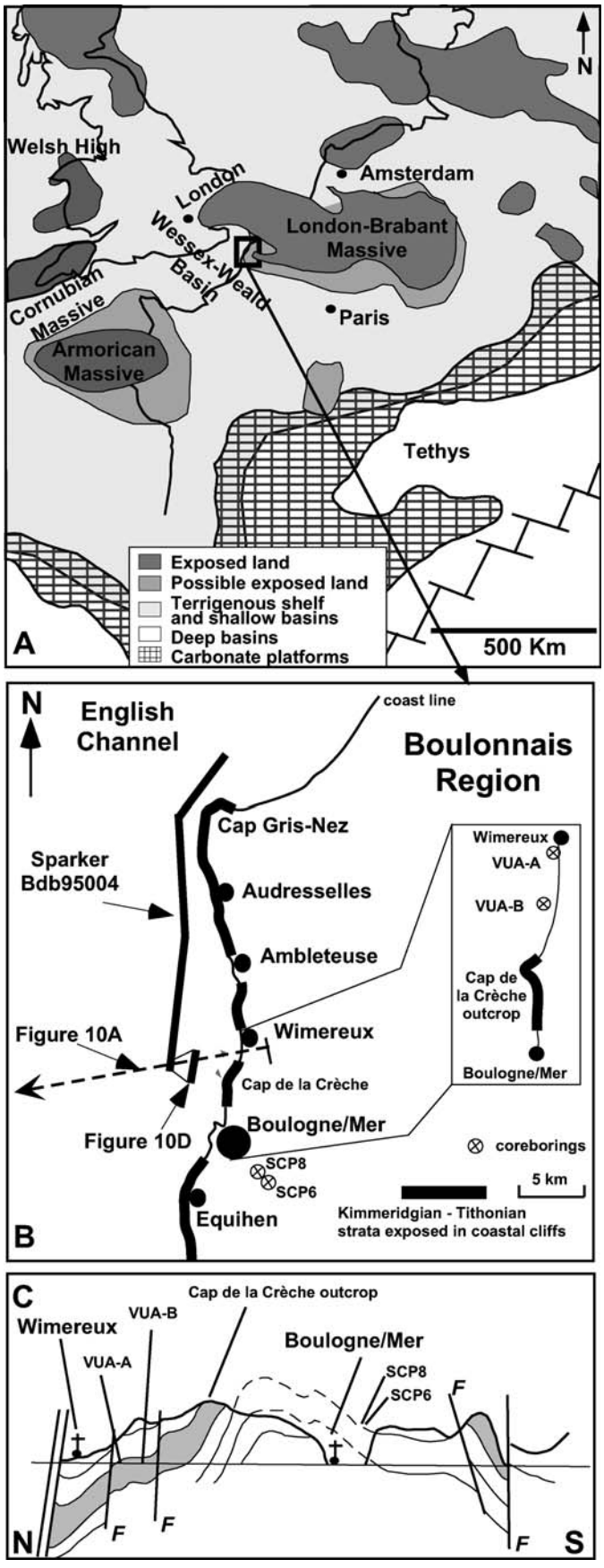

models are usually based on well-understood hydrodynamic processes (e.g., progressive sorting by Russell 1939 and stratal condensation by Crowley 1984), geometric rules (Bruun 1962; Steckler 1999), and diffusion rules (Kaufmann et al. 1992; Niedoroda et al. 1995). However, they generally lack quantitative information on lithology and physical properties, and they do not take into account diagenetic processes that ultimately have the largest impact on acoustic properties. Therefore, for numerical models to be directly applicable to seismic stratigraphic analyses of sedimentary basins, diagenetic processes must be integrated with "standard" modeling and data-assimilation efforts.

This study describes the essential integration of deposition of sediments and time-and-space-localized cementation processes to create a physical stratigraphic model in a sequence stratigraphic context that allows a quantitative seismic sequence stratigraphic interpretation and hence the identification and characterization of key diagnostic criteria of sharp-based shoreface deposits. This is done in four steps, which form the basic structure of this paper.

1. A paleogeographical reconstruction is performed, based on three sections in the Boulonnais natural research observatory (the outcrop and boreholes VUA-B and VUA-A; Figs. 1, 2, 4). This reconstruction is tied with more distal time-equivalent sections in England and is put in a sequence stratigraphic framework.
2. The depositional environment across a complete depositional ramp profile is physically quantified (Figs. 5, 6, 7).
3. Combining the quantified depositional environment with a quantification of the actual sediment and its evolution of physical properties deposited over time in these environments, a physical characterization of systems tracts and their key bounding surfaces in time and space allows the development of a quantitative mechanical sequence stratigraphic model of an Upper Jurassic epicontinental margin (Figs. 8, 9, 10).
4. The integration of this model with a seismic wavelet to create a synthetic seismic section allows a contrast comparison with real seismic data and the identification of key diagnostic criteria for sharp-based shoreface deposits (Figs. 10, 11). The application of this mechanical sequence stratigraphic concept to determine the origin and nature of seismic reflections serves as a missing link between outcrop and seismic sequence stratigraphy and may very well be more generally applicable.

GEOLOGICAL SETTING AND PREVIOUS WORK

During the Late Jurassic in Western Europe, organic-rich mudstones were deposited over large areas from the Barents Sea to the North Atlantic (e.g., The Kimmeridge Clay) in shallow epeiric seas (Proust et al. 1995). The partitioning of the northwestern European shallow basins is related to changes in the subsidence regime that occurred during the transition from initial rift to post-rift-drift conditions. Several phases of fault-controlled differential subsidence, acting on preexisting crustal lineaments, led to the development of a series of dominantly east–west trending asymmetric half-grabens and intervening highs (Taylor and Sellwood 2002) and basin-wide unconformities (e.g., Lower Oxfordian, Lower Tithonian and Early Aptian). In the Wessex–Weald Basin (west), passing the Boulonnais High (middle) and towards the Paris Basin (east),

←

FIG. 1.—**A)** Early Kimmeridgian paleogeography, after Schnyder et al. (2001). The box indicates the approximate area in part B. **B)** The Boulonnais Region: location of cliff outcrops, boreholes VUA-A and VUA-B, and the seismic line (Bdb 95004) are indicated (modified after Schnyder et al. 2001). **C)** A cross section along the cliffs of the Boulonnais where the locations of the boreholes are indicated (modified after Herbin et al. 1995).

five phases of basin fill are recognized: (1) a general onlap onto a Late Oxfordian unconformity during initial sea-level rise (*baylei* and *cymodoce* ammonite zones); (2) a gentle progradation until the uppermost part of the *eudoxus* ammonite zone; (3) a well-expressed onlap in the basinal English sections during relative sea-level rise, resulting in major accumulations of marine organic-rich sediment (*autissiodorensis* and lower *elegans* ammonite zones); (4) a renewed progradation followed by a retrogradation at the transition *elegans–scitulus* ammonite zones, and (5) a drastic fall in sea level associated with a major paleogeographic reorganization recorded only during the following relative sea-level rise during the *hudlestoni* and *pallasioides* ammonite zones (Proust et al. 1995).

In the Boulonnais area, the Upper Jurassic sediments were deposited close to the northeastern shoreline of the Wessex–Weald Basin at the edge of the London–Brabant Massif (Fig. 1A; Wignall et al. 1996). These sediments consist of shales and mudstones interbedded with calcareous sandstones, which represent potential reservoirs (Herbin et al. 1995; Gallois 1976). The overall low-energy depositional environment in the Wessex–Weald Basin resulted in the deposition of an aggradational stack of strata approximately 500-m-thick in the central part of the basin. The dominantly flat-lying architecture in this part of the basin decreases in thickness but exhibits little changes in lithological composition towards the margins (Taylor and Sellwood 2002). To explain the nature of the Wessex–Weald Basin fill in terms of relative sea-level changes, sequence stratigraphic concepts have been applied and tested by many authors (Wignall 1991; Herbin et al. 1995; Proust et al. 1995; Mahieux et al. 1998; Proust et al. 2001; Williams et al. 2001; Taylor and Sellwood 2002). Because the maximum overburden of the Upper Jurassic interval in the Boulonnais area reached a thickness of no more than 500 m (El Albani et al. 1993; Braaksma et al. 2003), the diagenetic alterations are eogenetic. Intense mechanical compaction, clay-mineral transformation reactions, burial quartz cementation, or substantial thermal alteration of organic matter have not occurred.

METHODS

Grain-Size Analysis and Carbonate Content

A total of 1187 samples were selected for the analysis of grain size and carbonate content. From the outcrop 440 samples were collected with an average spacing of 30 cm (Braaksma et al. 2003). From borehole VUA-A, 218 samples, and from borehole VUA-B 529 samples (samples spaced at approximately 25 cm), were selected from core. Grain size was measured using a FRITSCH A22 Laser Diffraction Spectrophotometer or "Laser Particle Sizer," which has a working range of 0.16–1400 μm. For details on the analytical procedure the reader is referred to papers by Konert and Vandenberge (1997), McCave et al. (1986), Loizeau et al. (1994), and papers cited therein.

The fraction of clay-size particles < 2 μm determined with the pipette gravitational sedimentation method (based on the Stokes sedimentation rates) corresponds with a grain size of 8 μm defined by the Laser Particle Sizer. The upper limit for clay-size fraction was set at 8 μm as a consequence of the measuring technique (Braaksma et al. 2003). The resulting volume percentage measurements were reduced to the following frequency class sizes: clay (< 8 μm), silt (8–63 μm), and sand (> 63 μm) using the Udden-Wenthworth grain-size scale (Prothero and Schwab 1996). Prior to grain-size analysis, the carbonate was removed from the sediment samples by treatment with an excess 1 M HCl solution, and all organic material was removed by boiling the sediment with deionized water with 0.3 gram $Na_4P_2O_710H_2O$. Grain-size analysis therefore provides the distribution of the siliciclastic sediment fraction only. The acid did not dissolve noncarbonate cements such as phosphate, pyrite, and glauconite. Samples containing these kinds of cemented nodular agglomerates were treated with a sonic dismembrator in order to break them up. Finally, by sieving the bulk granular material before analyzing it with the Laser Particle Sizer, as a consequence, any granular material larger than 1200 μm was excluded from further grain-size analysis.

Log-normal scales were used to compare different size distributions between samples, because they provide an equal emphasis on small differences in fine particles and larger differences in coarse particles. These log-normal grain-size distributions fall into four principal groups: (a) average size (mean), (b) spread of the sizes around the average (sorting), (c) symmetry or preferential spread to one side of the average (skewness), and (d) degree of concentration of the grains relative to the average (kurtosis). The logarithmical method of moments (Krumbein and Petijohn 1938; Friedman and Johnson 1982; Blott and Pye 2001) was used to fully describe the grain-size distributions and their vertical and lateral relationships.

Carbonate content is also related to the depositional system (Ketzer et al. 2003) and linked to properties such as acoustic behavior, permeability, porosity, and bulk density (Stafleu and Sonnenfeld 1994; Braaksma et al. 2003). Carbonate measurements followed the Scheibler procedure (Kenter et al. 1997). Samples were treated with hydrochloric acid (HCl) and the volume of carbon dioxide was determined and compared to a standard of 99% pure $CaCO_3$ and finally, corrected for atmospheric pressure and temperature. The weight percentage of carbonate was calculated from the carbon dioxide volume. The carbonate fraction has not been discriminated quantitatively for the contribution of particulate—or detrital—carbonate matter or carbonate as a precipitate or cement.

Gamma-Ray Spectrometry

On the outcrop sampling locations, the rock surface was cleaned by removing the first 10 cm of the weathered surface. Natural gamma radiation was measured using a Gr320 enviSPEC Portable Gamma-ray Spectrometer, and approximately 5 cm of stratigraphy was sampled at the same position as the gamma-ray measurement. The Gr-320 records total counts and counts in the ^{40}K, ^{238}U, and ^{232}Th fields during a pre-selected counting period of 120 seconds. The gamma detector was placed perpendicular to the bedding. As a result, adjacent beds will influence all measurements in beds thinner than 84 cm, which is the spatial sampling volume of the sensor. An average sampling interval of 30 cm was achieved for the whole cliff section.

In the boreholes natural gamma radiation was measured using wire-line logging tools. In borehole VUA-A, a natural gamma-ray detector was integrated with the density tool and collected total gamma counts data every 5 cm, whereas in borehole VUA-B a spectral gamma-ray tool (ANTARIS) was deployed with a sampling distance of 10 cm. The field of influence of the logging tools is approximately 80 cm.

Acoustic Properties

Acoustic velocity was measured using two methods: (1) ultrasonic compressional (P-wave) velocities were measured on core plugs as a function of pressure using a transducer that propagates a compressional (V_p) wave (500 kHz) along the plug axis. A source crystal was excited by a fast-rise-time electrical voltage pulse, which was recorded by a receiver crystal. The arrival time of the one-way travel time was picked when the signal exceeded a threshold voltage equal to 3% of the overall peak-to-peak amplitude of the first three half cycles of the signal. (2) On whole core, V_p was measured every cm using a core-line logging system (GEOTEK MSCL), following the same procedure as for core plugs. The center frequency of the pulse was 320 kHz, and measurements were performed under ambient pressure only. Precision of the measured velocities is within approximately 5%.

Porosity and density were measured using two methods: (1) On core plugs drilled from core and outcrop, bulk (saturated) density and porosity were measured. Plugs were weighed and dried for at least 72 hours at 70°C. Next bulk and dry densities were calculated from wet and dry

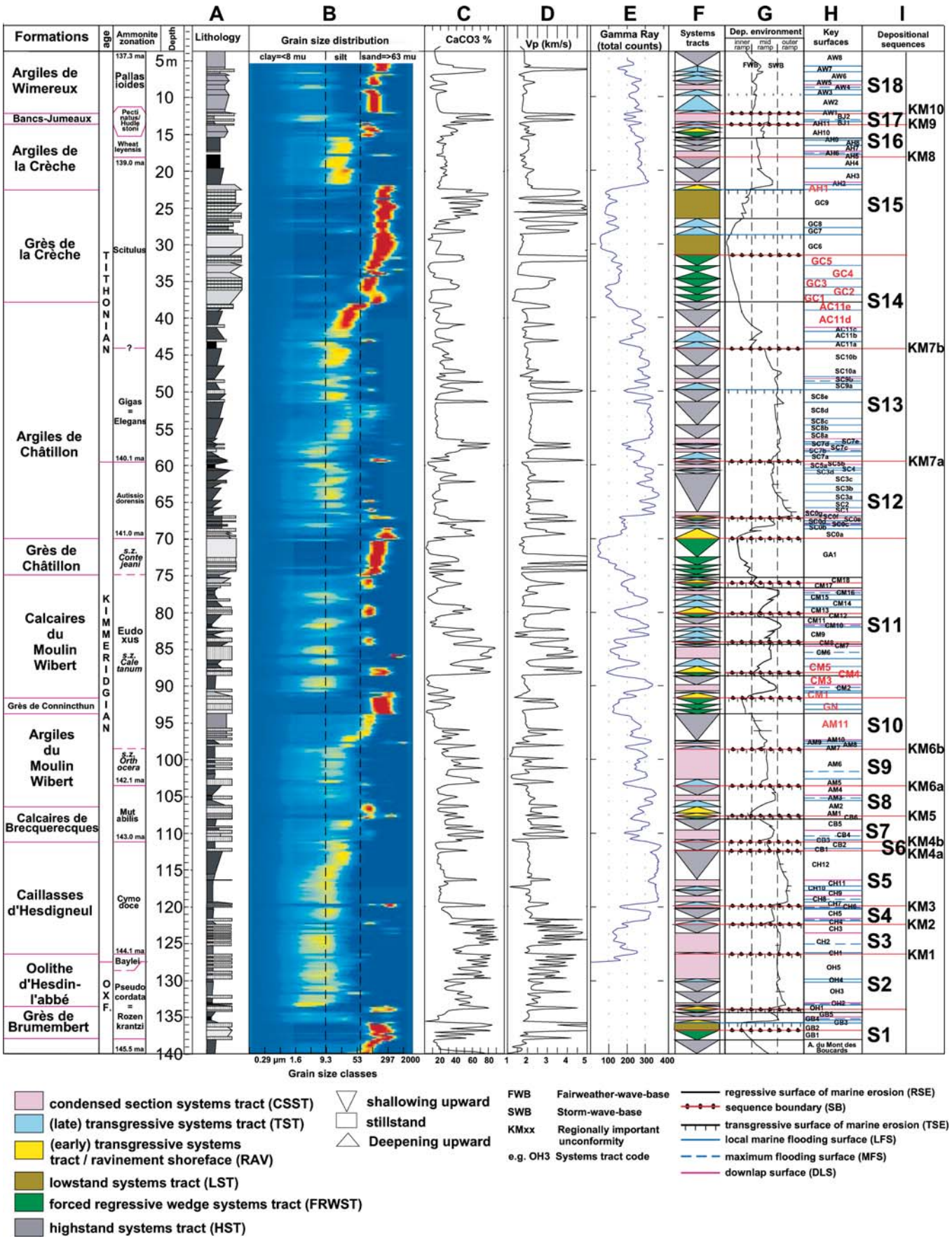
A
B
C
D
E
F
G
H
I
Formations
age
Ammonite zonation
Depth
Lithology
Grain size distribution
clay=<8 mu
silt
sand=>63 mu
CaCO3 %
Vp (km/s)
Gamma Ray (total counts)
Systems tracts
Dep. environment
inner ramp
mid ramp
outer ramp
Key surfaces
Depositional sequences
Argiles de Wimereux
Bancs-Jumeaux
Argiles de la Crèche
Grès de la Crèche
Argiles de Châtillon
Grès de Châtillon
Calcaires du Moulin Wibert
Grès de Conincthun
Argiles du Moulin Wibert
Calcaires de Brecquerecques
Caillasses d'Hesdigneul
Oolithe d'Hesdin-l'abbé
Grès de Brumembert
TITHONIAN
KIMMERIDGIAN
OXF.
Pallasioides
Pectinatus/ Hudlestoni
Wheatleyensis
Scitulus
Gigas = Elegans
Autissiodorensis
S.-z. Contejeani
Eudoxus
S.-z. Calcitanum
S.-z. Orthocera
Mutabilis
Cymodoce
Baylei
Pseudocordata = Rozenkrantzi
137.3 ma
139.0 ma
140.1 ma
141.0 ma
142.1 ma
143.0 ma
144.1 ma
145.5 ma
FWB
SWB
A. du Mont des Boucards
0.29 µm 1.6 9.3 53 297 2000
Grain size classes
20 40 60 80
1 2 3 4 5
100 200 300 400
S18
S17
S16
S15
S14
S13
S12
S11
S10
S9
S8
S7
S6
S5
S4
S3
S2
S1
KM10
KM9
KM8
KM7b
KM7a
KM6b
KM6a
KM5
KM4b
KM4a
KM3
KM2
KM1
condensed section systems tract (CSST)
(late) transgressive systems tract (TST)
(early) transgressive systems tract / ravinement shoreface (RAV)
lowstand systems tract (LST)
forced regressive wedge systems tract (FRWST)
highstand systems tract (HST)
shallowing upward
stillstand
Deepening upward
FWB Fairweather-wave-base
SWB Storm-wave-base
KMxx Regionally important unconformity
e.g. OH3 Systems tract code
regressive surface of marine erosion (RSE)
sequence boundary (SB)
transgressive surface of marine erosion (TSE)
local marine flooding surface (LFS)
maximum flooding surface (MFS)
downlap surface (DLS)

sample weights and measured cylinder volumes. Grain densities were derived by dividing the mass of the powdered samples by the volume using a Micrometrics AccuPyc 3200 helium pycnometer. Total porosity was calculated from bulk dry density and grain density. More detailed procedures are described by Carmichael (1990), Kenter and Ivanov (1995), and Braaksma et al. (2003). (2) On whole core, wet bulk density was measured every cm using a core-line logging system (GEOTEK MSCL). Porosity was calculated from gamma density using the grain densities derived from the grain-size distributions and measurements of bulk carbonate content by assuming a grain density of 2.712×10^3 kg/m^3 for the carbonate fraction, 2.575×10^3 kg/m^3 for the clay fraction, and 2.649×10^3 kg/m^3 for the sand fraction.

RESULTS

Lithofacies and Depositional Environments

The two boreholes (VUA-A and VUA-B) on the beach between Wimereux and Boulogne sur Mer complement the well-described and analyzed cliffs (Proust et al. 1993, 1995; Herbin et al. 1995; Wignall and Newton 2001), between Equihen and the Cap Gris Nez, about 25 km apart (Fig. 1B, C). Nearly continuous core of borehole VUA-A (recovery 90%) and VUA-B (recovery 93%), along with a suite of down-hole logging data, provide a comprehensive integration of geophysical, geological, and geostatistical parameters. Furthermore, borehole VUA-B penetrated down to a depth of 140 m, providing excellent-quality core and logging data from Tithonian strata, through the complete Kimmeridgian strata down to Upper Oxfordian strata (Fig. 2).

The Upper Jurassic sediment observed in the two boreholes, in the outcrops, and on the seismic reflection profile were deposited on a homoclinal ramp (Ahr 1973; Read 1985; Burchette and Wright 1992). The paleobathymetry (i.e., the energy of deposition with respect to fair-weather and storm-weather wave action) and the carbonate productivity (i.e., biological processes, light, etc.) control the depositional environment along a homoclinal ramp. Three depositional environments are recognized in the Boulonnais sections: (1) outer ramp below or at storm wave base with only episodic or no storm influence; (2) mid-ramp between storm wave base and fair-weather wave base, with storm-wave reworking and shell accumulations; (3) inner ramp above fair-weather wave base with sandy, rippled, and cross-bedded facies and with a marked increase in intensity of bioturbation (Schlirf 2003).

The 13 formations that are observed (Fig. 2) comprise 18 lithofacies that are organized into three main groups ranging from outer-ramp to inner-ramp environments. These lithofacies are briefly described and interpreted in Table 1 (see also Wignall et al. 1996; Proust et al. 2001; Wignall and Newton 2001).

Sequence Stratigraphic Interpretation and Paleogeographic Reconstruction

The 25-km-long north–south trending cliff outcrops (strata belonging to *mutabilis* to *pallasioides* ammonite zones) show an overall NE–SW proximal to distal trend, with the palaeoshoreline to the NE (Proust et al. 1995). On the basis of various sections exposed in these outcrops, a reconstruction of the geometry of sharp-based shoreface deposits in the Kimmeridgian–Tithonian strata of the Boulonnais was proposed by Proust et al. in 2001 (Fig. 3A). The 2 km field observatory described in this paper (between borehole VUA-A and the Cap de la Crèche outcrop; Figs. 1, 4) thus represents a laterally small, slightly oblique cross section of the depositional system (Wignall and Newton 2001).

Sequence stratigraphic analysis divides the stratigraphic record into depositional sequences (Fig. 3B), in which the sequence boundary is defined as a subaerial erosion surface (unconformity) or its correlative conformity (Mitchum et al. 1977). Five other types of key surfaces were identified in this study (Table 2 and Fig. 3B). Sequence boundaries mark an abrupt basinward shift in deposition and are therefore commonly interpreted from a sharp shallowing of facies across erosion surfaces. Major hiatuses are commonly developed across these kinds of surfaces, particularly on basin margins (Posamentier and Vail 1988). On a regional scale in and around the Weald Basin, ammonite zones are the most important constraint on the correlation of different geological observations from boreholes and cliff outcrops of the Upper Jurassic stratigraphy (Taylor and Sellwood 2002). The regionally important unconformities in Figures 2 and 4 are numbered following Taylor and Sellwood (2002).

The integration of information on grain size, natural gamma ray, and depositional facies in cores (Fig. 2) and outcrops (Figs. 1, 3A), allows a paleogeographical reconstruction and a placement of this reconstruction in a much more detailed sequence stratigraphic framework (Fig. 4) than presented by Proust et al. (1993, 1995), Herbin et al. (1995), Wignall (1991), Wignall and Newton (2001), Williams et al. (2001), and Tribovillard et al. (2001).

Systems Tracts

Five systems tracts (*sensu* Brown and Fisher 1977; Van Wagoner et al. 1988; Van Wagoner et al. 1990; Carter et al. 1998) are recognized in the Boulonnais area (Fig. 3): (i) lowstand (LST), (ii) transgressive (TST), (iii) condensed section systems tract (CSST), (iv) highstand (HST), and (v) the forced regressive wedge systems tract (FRWST). The LST overlies a sequence boundary (SB), the TST a transgressive surface (TSE), the CSST a local flooding surface (LFS), the HST a downlap surface (DLS), and the FRWST a regressive surface of marine erosion (RSE). These systems tracts are the elementary building blocks of the 18 depositional sequences, which occur within the cored interval and are partly exposed in the fresh cliff outcrops.

In the Boulonnais area, the LSTs (brownish in Fig. 2F) exhibit progradational and/or aggradational geometrical relationships and are mainly composed of inner-ramp sediment (Fig. 2G; Table 1). It is bounded below by a sequence boundary and at the top by a transgressive surface of marine erosion (Fig. 2H). It represents a time of the maximum basinward shift of depositional environment followed by a shoreline built out before shoreline retrogradation. The LSTs are relatively coarse-grained (Fig. 2B), exhibit variable but overall high bulk $CaCO_3$ content (Fig. 2C) and high acoustic velocities (Fig. 2D), show low gamma ray response (Fig. 2E), and are observed only in sequences S1 and S15 (Fig. 2I).

The TSTs (light blue in Fig. 2F) are thin and deepen upsection from inner- to mid- or outer-ramp paleoenvironments (Fig. 2G). In the Boulonnais area the last stage of retrogradation is typified by the shoreface ravinement of earlier-deposited shoreface sands and muds

←

FIG. 2.—Borehole VUA-B. **A)** lithologic column (black, shales and muds; gray, sands; vertical stripes, carbonaceous intervals). The width of the lithologic column indicates grain size with the exception of carbonaceous intervals. **B)** Grain-size distribution. Color-coded is the frequency of relative occurrence of siliciclastic material in predefined grain-size classes (56 in total). The relative abundance of each size class increases going from deep blue to deep red. Shoaling events are observed as well as major breaks in shoaling trends. Indicated on the top are the boundaries for clay (< 8 μm), silt (> 8 μm and < 63 μm) and sand (> 63 μm). **C)** Bulk weight percentage $CaCO_3$. **D)** Acoustic velocity V_p (km/s). **E)** Natural gamma wire-line log data in total counts. **F)** Sequence stratigraphic interpretation. **G)** Depositional environment, where only regressive surfaces of marine erosion, sequence boundaries, and transgressive surfaces of marine erosion are indicated. **H)** Key surfaces and systems tract labels. **I)** Interpreted depositional sequences S1–S18. Indicated are regionally important stratigraphic unconformities (see text for discussion).

TABLE 1.—*Facies descriptions and interpretation of the main lithofacies observed in the Boulonnais natural observatory.*

Medium- to coarse-grained bioclastic sandstone beds with planar lamination, low-angle truncations, and swaly cross-stratification. ***High energy upper shoreface in a beach and or barrier island system.***	F1	INNER-RAMP
Same as F1 but unevenly truncated by channels underlined by a centimeter-thick layer of granules and pebbles of quartzites, sandstones, and cherts or by a monospecific oysters-rich shell lag. ***Same as F1. Tidal (?) channels.***	F2	
Decimeter-scale, fine- to medium-grained, carbonaceous and bioclastic sandstone beds. Simple to compound trough cross-bedding. Domichnia and fugichnia of the *Skolithos* ichnofacies (*Ophiomorpha, Teichichnus, Rhizocorallium, Diplocraterion* and *Skolithos*). ***High-energy, middle-shoreface deposits. Large simple to compound sand waves.***	F3	
Centimeter-thick, alternating fine-grained sandstone beds and shales (lenticular to flaser and wavy bedding) including lignite fragments. Current, combined wave-current ripples and hummocky-cross stratification frequently reworked by bioturbation. ***Wave-dominated lower-shoreface deposits.***	F4	
Massive, light-gray silty to sandy shales with lignite fragments and rare pelecypod debris. The bioturbation may preserve some fuzzy remains of lamination. Occurrences of glauconite, pyrite, and phosphate. ***Restricted, shore-proximal muds***	F5	
Sandy, bioclastic, bioturbated (oblique to vertical) limestone with large thick sheltered bivalvia and gastropods. The most sand-rich facies exhibit some crude trough-cross-bedding and planar lamination with low-angle truncations. Breccias, slumps. ***Mid-energy, close to wave base, offshore marine. Shifted shoals complex or fringing, prograding skeletal sand banks. Front slope resedimentation.***	F6	
Bioturbated, fine-grained sandy limestone beds with disarticulated, thin-shelled bivalvia. Some horizontal to wavy laminations and some fuzzy remains of wave ripple forms laminations disrupted by burrowing mottling. Some glauconite sand, drift wood, phosphate. dissolution breccias. ***Mid-energy, lower shoreface, at wave base ramp floor***.	F7	
Bioturbated, dark-gray silty marly shales with some disarticulated small size shell debris. Some glauconitic sands, lignite fragments, and ferruginous to phosphatic impregnations of subautochtonous shell pavement of large infaunal bivalvia. ***Low energy, nutrient-rich, shore-proximal below normal wave base, lime muds, slow accumulation (authigeneses), and winnowing (shells pavements). Lower shoreface to upper offshore.***	F8	MID-RAMP
Bioturbated, decimeter-scale coquinoid mudstone beds (thickness of facies equals bed thickness) with disarticulated, unsorted clusters of *Nannogyra virgula* in the Kimmeridgian, and during the Tithonian, undifferentiated pelecypods. In the latter case, sediment is often reworked. ***Low-energy (restricted?), offshore marine paleoenvironment. Subautochthonous communities (2) reworked by deep infaunal bioturbation.*** **Nannogyra virgula** ***seems to be well adapted to substrate during their adult life (planctonic larvae, cemented on firm substrate youth) helped by a self-cleansing mechanism (3). The apparent lack of hydrodynamical processes, the presence of*** **Chondrites,** ***and dissolution cracks argues for restriction and low-oxygen sea-bottom conditions.***	F9	
Thoroughly bioturbated marly shale beds with few thin-shelled bivalvia, disarticulated and disturbed. Thin shell debris may be arranged along low-angle, planar lamination or hummocky cross-stratification. ***Interpretation same as F12.***	F10	
Coquinoid shales concentrated with shells of pelecypods (*Nannogyra virgula* in the Kimmeridgian). The two valves of the coquina are preserved, disarticulated, but standing in the disequilibrium concave-up position. The sizes of the shells are very similar. Planar to low-angle lamination. ***Deep, soft substrate, ramp floor episodically provided with*** **Nannogyra virgula** ***organisms by seaward-flowing storm surges or currents, and concentrated by secondary elutriations on a current-swept floor. The homogeneous sizes of the shells and the preservation of the two valves with some in concave-up position argues for in-place elutriation.***	F11	
Skeletal wackestone with some thin shelled, whole-bodied epifaunal pelecypods in a random position and a few, well preserved, poorly diversified, standing in anatomic connection and life-up position, deep infaunal assemblages (*Trigonia*, *Gervillella*). Most of the latter underlie ferruginous horizons ***Low-energy, restricted (1), deep, offshore marine below-storm-wave-base lime muds.***	F12	
Centimeters-thick and some decameters to hectometers in lateral extent (thickness of facies equals bed thickness) fine- to medium-grained carbonaceous sandstone beds with an undulatory or flat erosional sole underlain by infaunal pelecypods. Most of these beds are graded, massive, planar laminated or hummocky-cross-stratified. ***Episodic, high-energy, storm-dominated open marine conditions. The paleodepth evolves progressively in the stratigraphic record from the upper part of the lower offshore (4) to the base and the middle parts of the upper offshore.***	F13	OUTER-RAMP
Same as F13; The sandy fraction is replaced by large concentrations of small coquinas only a few millimeters thick. Most of the beds are graded. ***Episodic, high-energy, storm-influenced open marine conditions. The storm-graded layers result from massive sediment deposition by seaward-flowing storm-surge currents which may occur far below normal storm wave base.***	F14	
Massive dark gray marly shale beds with local occurrences of silt–clay, thick–thin laminae couplets. ***The thick–thin couplets are interpreted as the result of episodic deposition of a thin blanket of sediment on the sea floor due to recurrent flood events.***	F15	
Massive dark gray marly shale beds with shallow infaunal, small, millimeter-scale, thin-shelled, disarticulated bivalvia (*Lucina*, *Nannogyra*). *Cruziana* ichnofacies (*Planolites*, *Thalassinoïds*). ***Low-energy, offshore marine ramp environment. Soft substrate conditions colonized with shallow infaunal suspension feeders (6) prevail.***	F16	
Organic rich, dark, microlaminated shale beds with unevenly spaced millimetric horizons of small size, shallow burrowing pelecypods. The main characteristics of the biological assemblage are: the very low diversity, the lack of deposit feeders and benthic larvae (prodissoconch bivalvia), and rare epifauna. ***Low-energy, offshore marine, episodically starved and dysaerobic ramp floor. Seasonal to annual oxic and anoxic conditions related to the very high frequency of shallow infaunal endobenthos mortality events (shells lag–mud couplets) (7)***	F17	
Couplets of micritic limestone and marly beds, bioturbated and fossiliferous (pelecypods, brachiopods, echinoderms, bryozoans, foraminifera). Characterized by marine hardgrounds and other evidence of omission surfaces. ***Low-energy, off-shore marine ramp environment, recording periodic clastic sediment starvation.***	F18	

1. From Wilson (1975); Flügel (1982) Hunt and Tucker (1992). 2. See also Ziegler (1969) and Ager and Wallace (1966). 3. From Seilacher (1984); Fürsich and Oschmann (1986) and Stenzel (1971). 4. Aigner (1985). 5. Guillocheau (1990). 6. Fursich and Oschmann (1986). 7. Oschmann (1990).

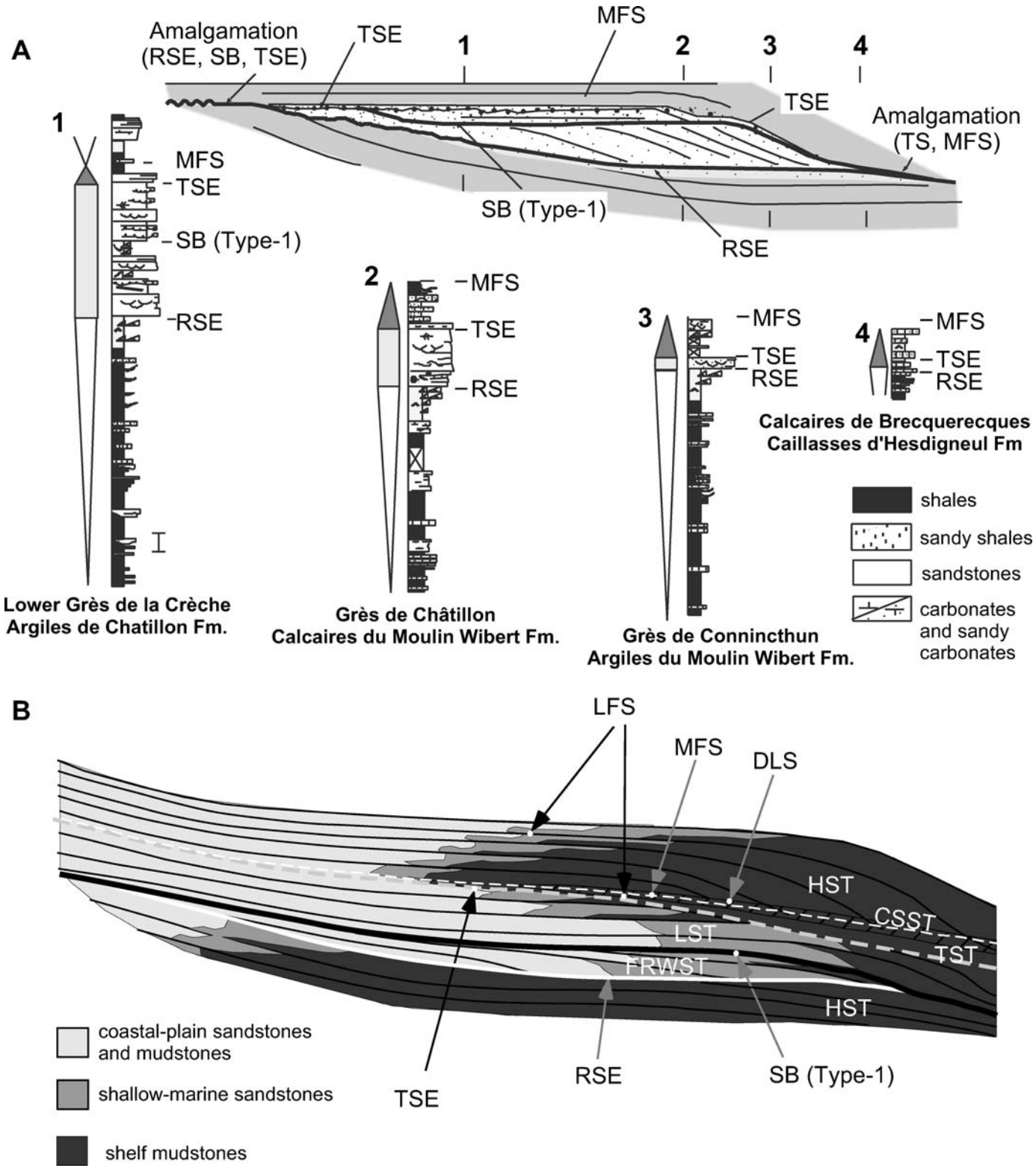

FIG. 3.—Previous work in the Boulonnais and sequence stratigraphy. **A)** Schematic reconstruction of the geometry of the sharp-based shoreface deposits in the Kimmeridgian and Tithonian strata of the Boulonnais. This is a composite reconstruction based on sections in the different kinds of sharp-based shoreface deposits superimposed on the large-scale progradational trend of the Kimmeridgian and Tithonian section along the 25 km of outcrops in the Boulonnais area. Each section, 1, 2, 3, and 4, belongs to different sharp-based deposits (modified after Proust et al. 2001). A key for the abbreviations is given in Figure 2. **B)** Stratal patterns of a sequence deposited in a basin with a ramp margin (modified after Posamentier et al. 1988). Indicated are the key surfaces and the dimensions and positions of the systems tracts within a full depositional sequence. A key for the abbreviations is given in Figure 2.

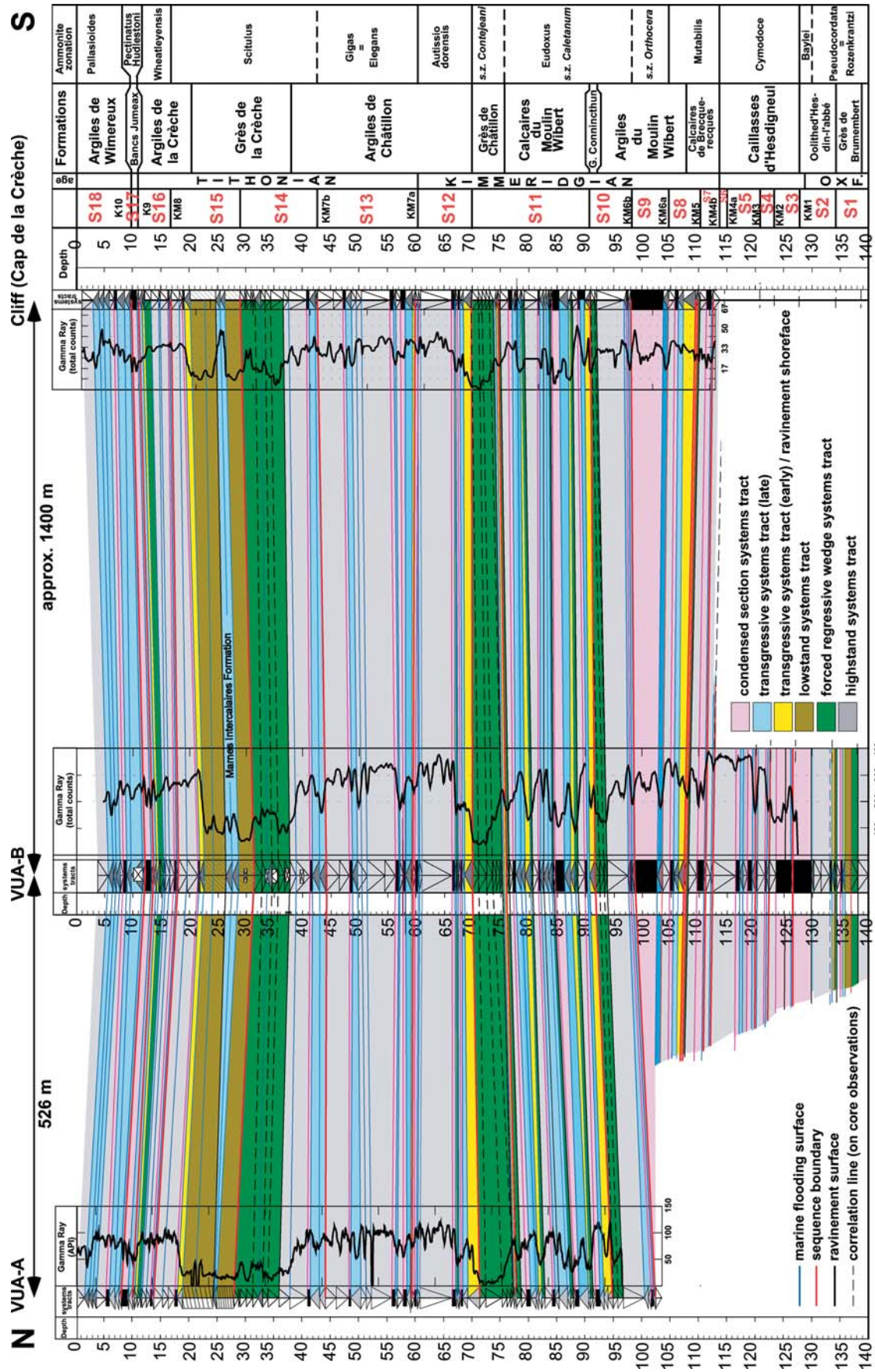

FIG. 4.—The paleogeographic reconstruction between the boreholes and the Cap de la Crèche outcrop section. Gamma-ray logs are displayed along with the sequence stratigraphic interpretation. The correlation, however, is based on the integrated information on grain-size distribution, carbonate content, and gamma ray. Sequences S1 to S5 have been correlated with the SCP6 and SCP8 cores described by Schnyder et al. (2001) (see Fig. 1 for location). The difference in thickness of the silty shale interval within the Grès de Brunembert Formation (1.5 m in VUA-B vs. 0.45 m in SCP8) suggests a SN proximal to distal trend in deposition. Correlation of VUA-B and the cliff outcrop reveals thickness differences that suggest a NS proximal to distal trend for the Mutabilis zone. A fall in relative sea level associated with the KM 4b sequence boundary was most likely the primary control on the deposition of muddy siltstones in this ammonite zone. Similar time-equivalent sandstone deposits (the Elsham Sandstones) have been reported in England by Taylor and Sellwood (2002). Correlation of the FRWST of S11 (Grès de Châtillon, GA1) shows that it is thickest in the more distal north, decreasing in thickness towards the south, filling up most of the accommodation space associated with the genesis of the KM6b sequence boundary. The Grès de Conninchthun and Grès de Châtillon sandstone bodies can be correlated with the KC 26/27 and KC30 in the sections observed in England (Taylor and Sellwood 2002). For sequences S12–S18 a NESW direction of progradation is inferred from V-shaped geometries in between the three sections. This architecture is most prominent in S14, S15, and S18.

TABLE 2.—*Key surfaces identified and used in the sequence stratigraphic analysis of the Boulonnais natural observatory.*

	Diachronous Physical Surfaces	Interpretation
1	Erosional truncations of shoreface deposits or channelizezzd tidal-sandstone bodies, overlain by high-energy, coarse-grained shoreface sands.	Transgressive surface of marine erosion (TSE): surface produced by wave ravinement during marine transgression
2	Erosional truncations of beach and shallow marine sediment by thin wave-reworked sediments and >tidal-inlet deposits (channel and flats) with scarce rootlets	Exposure surface corresponding to a sequence boundary unconformity (SB)
3	Erosional truncations of shale or sandy shale with scarce flaser bedding, overlain by shoreface sand.	Regressive surfaces of erosion (RSE): surfaces produced by wave action zduring regression
4	Non-erosional surface overlain by lithofacies that generally show coarsening up	Downlap surfaces (DLS): surfaces associated with little to no erosion, zrepresenting changes in sedimentation rates
5	Erosional truncations of marine strata overlain by deeper marine vstrata without significant erosion that correlate landward to TSEs	Conformable marine flooding surfaces: Local flooding surfaces (LFS)

1. *sensu* Van Wagoner et al. (1988). 2. *sensu* Proust et al. (2001). 3 *sensu* Hunt and Tucker 1995; 4. *sensu* Carter et al. (1998); 5. *sensu* Carter et al. (1998).

(RAVs). Elsewhere the bases of the TSTs are usually marked by a shell lag, millimetric pebbles, or a centimetric thoroughly bioturbated glauconitic sandy horizon enriched with shell debris, lignite fragments, and ferruginous to phosphatic impregnations of subautochthonous shell pavements of large infaunal Bivalvia. These basal deposits may be generated either by a landward or upward shift of wave-base forming a surface that is predominantly erosional, or by a rapid marine flooding with a surface formed mostly by sediment starvation. The TSTs usually show a fining-upward trend in grain size (e.g., SC9a in Fig. 2B, H), are highly variable in bulk $CaCO_3$ content (Fig. 2C), and usually show an increase in gamma-ray counts from base to top (Fig. 2E) and overall low V_p (Fig. 2D).

The CSSTs (pink in Fig. 2F) are discrete stratigraphic units and are bounded at the base by a local flooding surface (LFS) and at the top by a downlap surface (Carter et al. 1998). A CSST constitutes a continuation of the condensed section (Baum and Vail 1988), as sedimentation rates at the toe of HST prograding clinoforms remain low. In the Boulonnais area the CSSTs are characterized by marine hardgrounds and other evidence of omission surfaces like calcareous sediment, authigenic minerals such as glauconite and phosphate, and high organic matter. The maximum flooding surface (MFS) is located within this systems tract, where in some cases it can correspond with a physical TSE/LFS (Fig. 2G). This occurs only on more proximal parts of a shelf. For locations farther offshore, the maximum flooding surface is separated from the LFS by a thin layer of mid-cycle condensed sediment (e.g., Carter et al. 1998).

The HSTs (gray in Fig. 2F) are a few meters to more than ten meters thick, progradational and gradually shallowing upward from deep outer-ramp environment to shallow mid-ramp or inner-ramp depositional environments (Fig. 2G). The top of the HSTs is sandy, and it is bounded at its base by a downlap surface (Fig. 2H). Overall, the HSTs are relatively fine-grained (Fig. 2B), characterized by overall low $CaCO_3$ content, with the exception of graded shell beds (Fig. 2A, C), low V_p, with the exception of graded shell beds and highly cemented siltstone ribs (Fig. 2D), and show high gamma-ray counts (Fig. 2E).

The FRWSTs (green in Fig. 2F) are separated from the HSTs by a clearly defined erosional surface (RSE) caused by the basinward and downward shift of wave-base (Hunt and Tucker 1992; 1995). This bounding surface is often marked by a sharp increase in grain size (e.g., 93.72 m in Fig. 2B) and usually constitutes the sharp transition from mid-ramp to inner-ramp depositional environments (Fig. 2G). A RSE can be correlated for tens of kilometers and is sometimes chosen as a formation boundary (e.g., Argiles de Moulin Wibert/Grès de Connincthun, Calcaires de Moulin Wibert/Grès de Châtillon, Argiles de Châtillon/Grès de la Crèche). The FRWSTs coarsen upward (Fig. 2B), and exhibit variable $CaCO_3$ content (Fig. 2C) and V_p values (Fig. 2D) and intermediate to low gamma-ray counts (Fig. 2E).

Many depositional sequences (e.g., S9, S17; Fig. 2I) are incomplete where the SB is coincident with the TSE and/or the RSE (Fig. 2H). In those cases, the LST is missing or subtly recorded by a single thin bed (e.g., S2–S10; Fig. 2I). These single beds generally have an erosional base overlain by a silty and/or sandy bed and have an average thickness of 20 cm. They contain reworked phosphates and glauconite, shell debris, and considerable amounts of clay. The reworked phosphate grains and shell debris are interpreted to indicate periods of wave or current agitation (Gallois and Cox 1976; Gallois 2000), and reflect a lowering of storm wave base in response to relative sea-level fall. The silty beds overlying the erosion surface in more distal settings have been interpreted as transgressive lags (Gallois 2000).

Quantitative Integration of Texture and Mineralogy

To quantitatively characterize the key surfaces and systems tracts of the Late Jurassic ramp deposits, a cross plot of mean grain size and sorting (the standard deviation around the mean) of samples taken from cores and outcrop with an average spacing of 25 cm (resulting in multiple samples from different systems tracts, deposited at different locations on a ramp profile) provides a tool to examine shoreface composition in a continuum of possible sedimentological parameters and/or lithofacies, as well as their position within the stratigraphic record. It is important to note that in order to employ the entire grain-size sample population, all statistics were calculated using the logarithmic method of moments (Blott and Pye 2001). Sorting is expressed both numerically and descriptively: with increasing values of sorting the distributions are moderately sorted (values ranging from 0.5 to 1), poorly sorted (values ranging from 1 to 2), or very poorly sorted (values larger than 2).

In Figure 5A the skewness (the symmetry or preferential spread to one side of the average) is contoured in the sorting–mean space. Following the terminology proposed by Blott and Pye (2001), four zones can be identified: where grain-size distributions contain a tail of coarser particles, the distribution is coarse skewed (-1.3 to -0.43); where grain-size distributions do not contain any tails at all, the distribution is symmetrical skewed (-0.43 to 0.43, where 0 skewness values indicate perfect symmetry); where grain-size distributions contain an excess of fines, the distribution is fine skewed (0.43 to 1.3); very fine skewed distributions contain a low amounts of excess fines in their tails (> 1.3).

In Figure 5B the kurtosis (the degree of concentration of the grains relative to the average) is contoured in the sorting–mean space. Five zones can be identified: where grain-size distributions are relatively flat, the distribution is very platykurtic (< 1.7); where grain-size distributions are less flat, the distribution is platykurtic (1.7–2.55); where distributions approach a perfect normal distribution, the distribution is mesokurtic

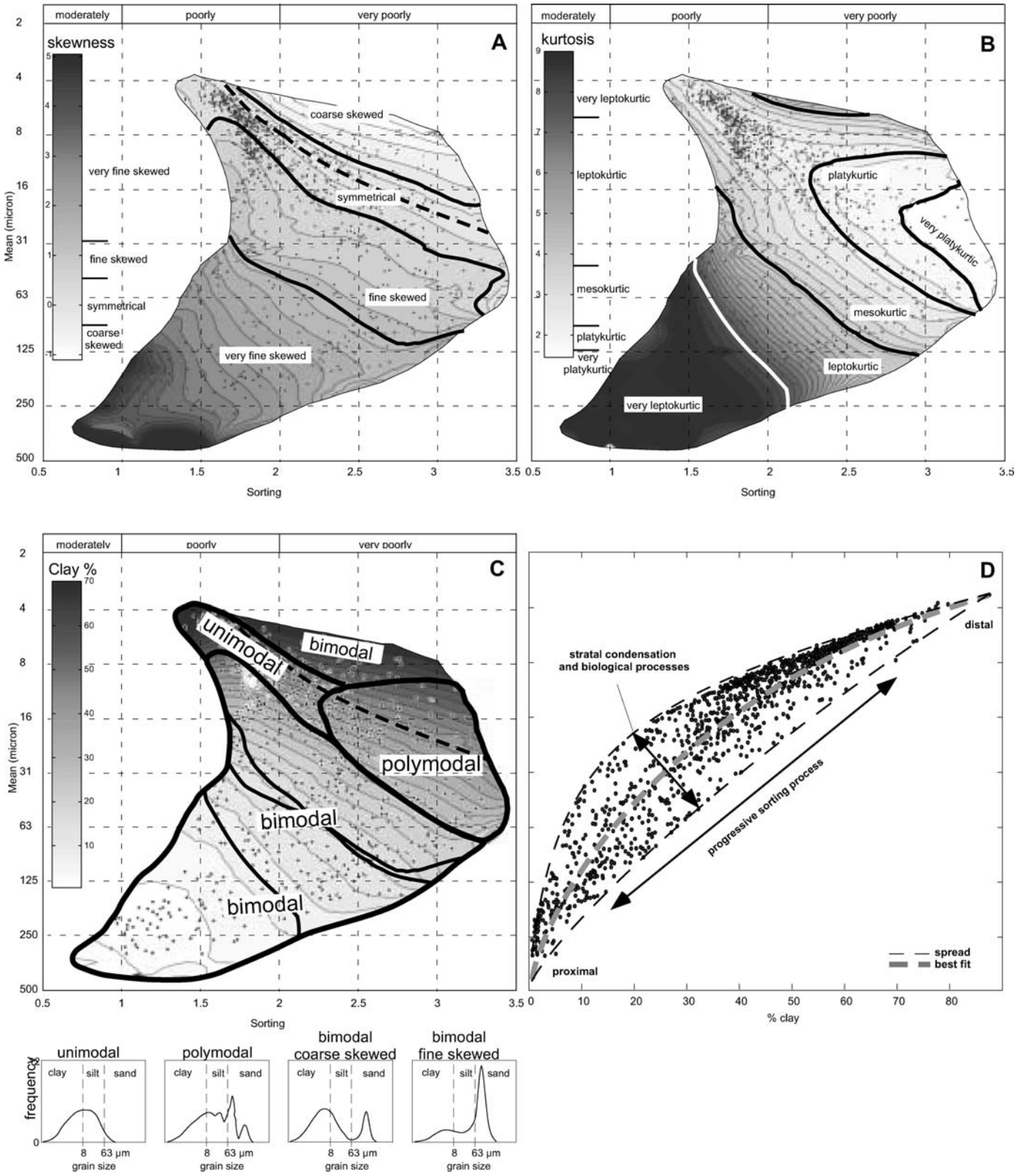

FIG. 5.—Texture, mineralogy, and depositional environment. **A)** Cross-plot of sorting (the spread of the sizes around the average) against mean grain size over which the skewness (the symmetry or preferential spread to one side of the average) is contoured. **B)** Same as part A but now kurtosis (the degree of concentration of the grains relative to the average) is contoured in the sorting–mean space. **C)** Same as part A but now the volumetric percentage clay (grains < 8 µm) is contoured. Combining the skewness and kurtosis contours, the modality of grain-size distributions fall into four main groups, indicating energetic differences in depositional environments. **D)** Cross-plot of volumetric percentage clay and mean grain size, illustrating the processes working on the sea floor (see text for discussion).

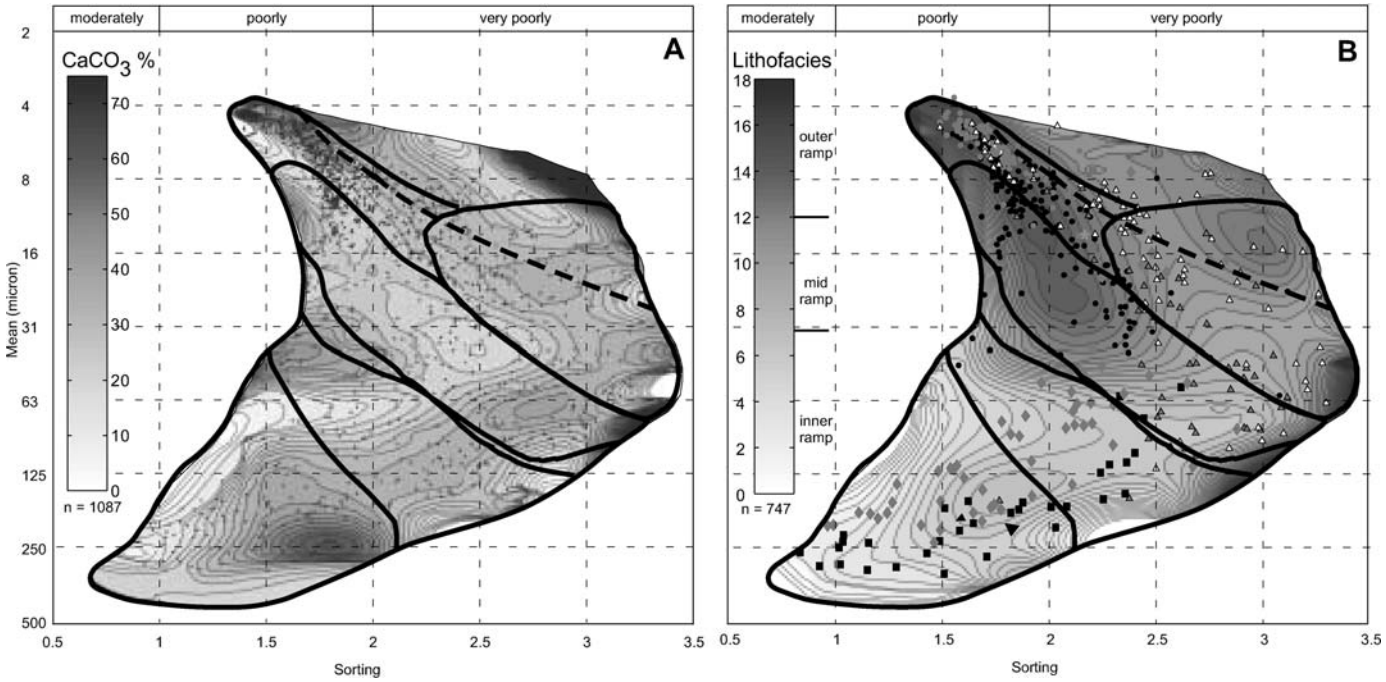

FIG. 6.—Texture, mineralogy, and depositional environment. **A)** Same as in Figure 5A but now the weight percentage $CaCO_3$ is contoured. Indicated are the important skewness and kurtosis contours. **B)** Same as Part A but now lithofacies coding (see Table 1) is contoured. Indicated are the important skewness and kurtosis contours (see text for discussion).

(2.55–3.7); where distributions are relatively peaked, it is leptokurtic; and where distributions are strongly peaked, the distribution is very leptokurtic.

As previously noted by Blott and Pye (2001), care must be taken when interpreting the skewness and kurtosis statistics when sediments are not unimodal. Where unimodal distributions may reflect equilibrium sediment (a specific grain-size class of the bulk flux that is in transit with a statistical spread around its mean, deposited at a specific location on a ramp profile at a certain time under the influence of size-selective transport), polymodal distributions may reflect admixtures of equilibrium sediment and reworked coarser sediment populations (Tamura et al. 2003). Most sediment in the Boulonnais study area show bimodal distributions, and nearly all sample distributions (regardless of de-

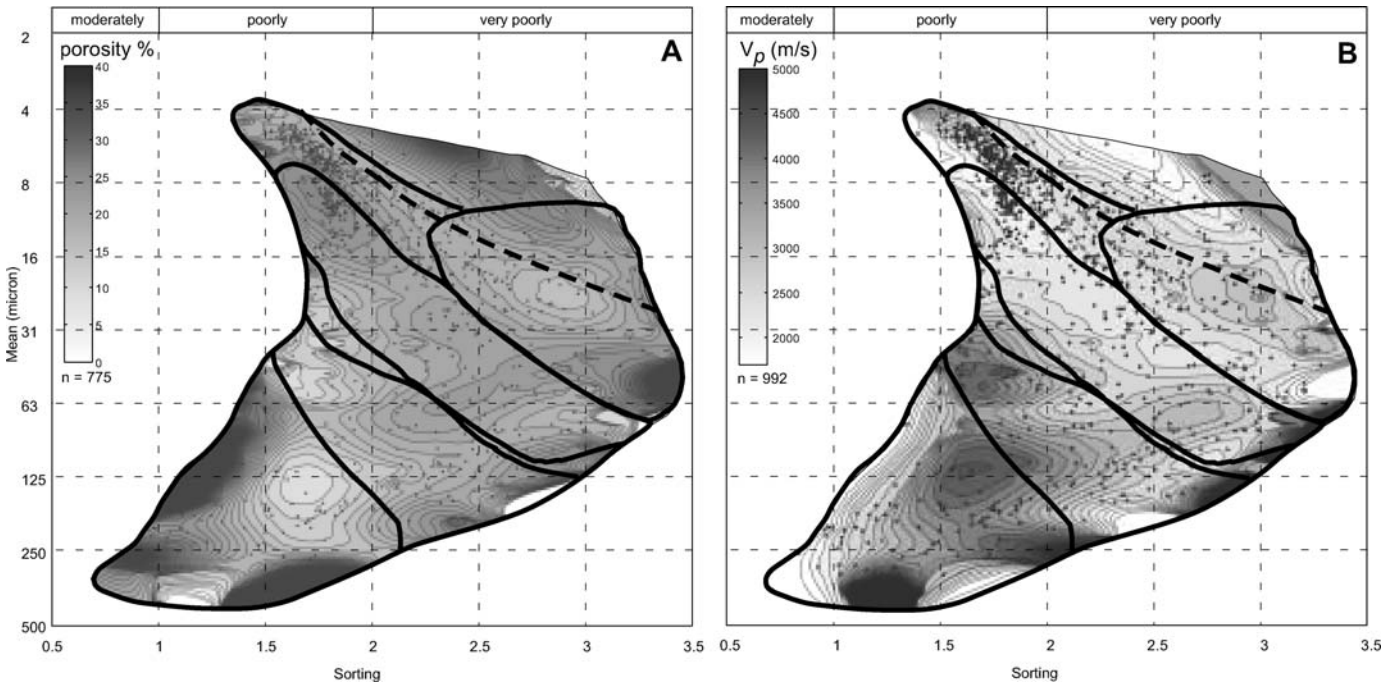

FIG. 7.—Texture, mineralogy, and acoustic properties. **A)** Same as in Figure 5A but now porosity (%) is contoured. Indicated are the important skewness and kurtosis contours. **B)** Same as Part A but now V_p (km/s) is contoured. Indicated are the important skewness and kurtosis contours (see text for discussion).

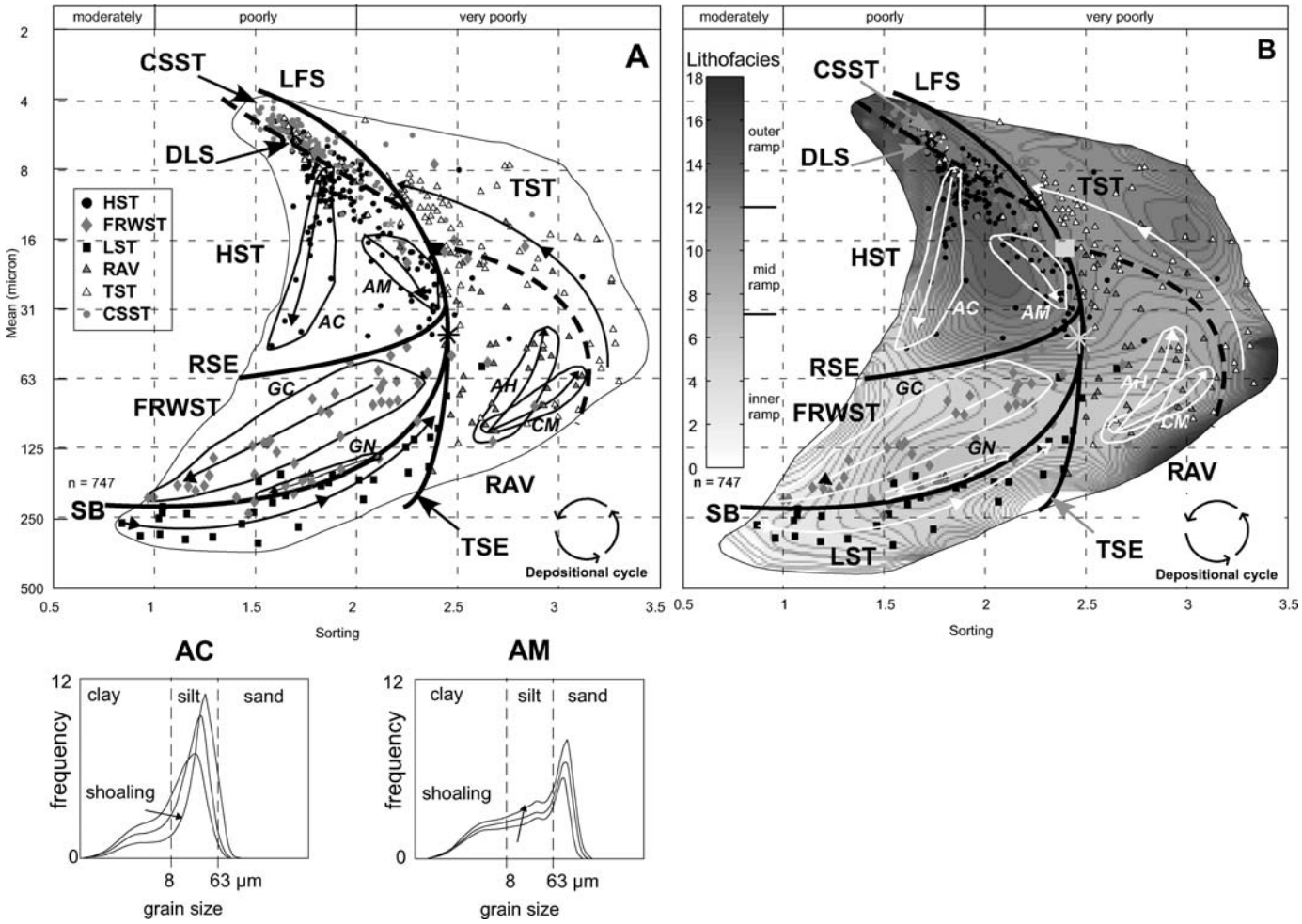

FIG. 8.—Systems tracts: textural, diagenetic, and petrophysical characterization. **A)** Cross-plot of sorting versus mean grain size for all 18 sequences. Color and symbol codes represent the interpreted systems tracts. Two end members of shoaling events (arrows indicate direction) are indicated in the generalized highstand systems tract (HST), forced regressive wedge systems tract (FRWST), and ravinement shoreface (RAV) spaces: proximal depositional environments are inferred for AC, GC, and AH, distal depositional environments are inferred for AM, GN, and CM. The small panels below illustrate the different shoaling characteristics for proximal (AC) and distal (AM) depositional environments with respect to the paleoshoreline (see text for discussion). Key stratigraphic surfaces bound the systems tracts: RSE = regressive surface of marine erosion; SB = sequence boundary; TSE = transgressive surface of marine erosion; LFS = local flooding surface; DLS = downlap surface. **B)** Same as in Figure 6B but now overlain by the sequence stratigraphic model as defined in Part A.

positional settings) exhibit a relatively fine-grained population in their tails, suggesting a continuous background supply of mud over larger parts of the ramp profile, which is not uncommon for these types of margins (Overeem et al. 2003).

Combining the major contour lines of skewness and kurtosis in the sorting–mean space and contouring the volumetric percentage of clay in this space (Fig. 5C), the following subdivision in modality of the grain-size distributions of Oxfordian to Tithonian strata in the Boulonnais area can be made:

1. Bimodal, fine-skewed distributions show the largest variability in terms of mean grain size and sorting. The skewness and kurtosis statistics provide the boundaries of their occurrence in the sorting–mean space.
2. Polymodal distributions are very poorly sorted and the boundaries are provided by the kurtosis statistics (Fig. 5C). Platykurtic distributions contain a range of modes of grain sizes that in the calculation of kurtosis of a specific grain-size sample are expressed as relatively flat as opposed to a perfect normal distribution.
3. Unimodal distributions are moderately sorted, the boundaries of occurrence in the sorting–mean space are provided by the combination of the skewness and the kurtosis statistics and their grain-size distributions are highly symmetric around their means.
4. Bimodal, coarse-skewed distributions show little variability in the amount of clay but have a large variability in sorting. In this type of distribution the equilibrium sediment are mixed with minor amounts of coarse material, which most probably has an origin in the reworking of underlying strata or that consists of small (< 1200 µm) noncarbonate cemented agglomerates, causing the large variation in sorting. The coarser the grains of the possibly reworked sediment, or agglomerates that are mixed with equilibrium sediment, the poorer the sorting of the bulk sediment.

Texture, Mineralogy, and Depositional Environment

As defined by the early sequence stratigraphic workers, the depositional system is an assemblage of genetically related facies (Fisher and

TABLE 3.—*Geological and petrophysical characterization of systems tracts observed and interpreted in the Boulonnais observatory.*

systems tracts	itho-facies	spatial characterization granulometrics	spatial characterization carbonate content	temporal characterization diagenesis	acoustic properties
SB					
LST	F1–F6	slightly fining upwards accompanied with a decrease in sorting preserved only in proximal settings	highly variable $CaCO_3$ contents, where concentration of bioclasts occurs in swash x-stratified and or in tabular x-stratified shell gravels	bleached zones (“whitecaps”) due to lignite diagenesis formation of spheroidal concretion due to prolonged residence times in beneath flooding surfaces	porous and low V_p at the base, but with slowly rising sea level (and flooding) rapid porosity reduction leading to high V_p at an early diagenetic stage
TSE					
TST (early) = RAV	F5–F10	fining upwards accompanied by a decrease in sorting *proximal:* thin and poorly sorted *intermediate:* thickest and most poorly sorted *distal:* thin and poorly sorted	multiple flooding events = stacking of thin parasequences where at the boundaries bioclastic concen tration occurs bioclastic storm-related event beds	*proximal:* minor diagenetic carbonate *intermediate:* thin cemented (discontinuous) horizons *distal:* minor diagenetic carbonate	compartmentalized *proximal:* porous, low V_p *intermediate:* compartmentalized *distal:* intermediate to low porosity and elevated V_p
LFS					
TST (late)	F11–F14	fining upwards poorly to very poorly sorted no apparent difference between proximal or distal settings unimodal grain-size distributions	overall low $CaCO_3$ content bioclastic storm-related event-beds	minor diagenetic alterations due to short residence times, low permeability in combination with the isolated nature of shell beds	overall intermediate to low porosity (intermediate to high V_p) except for storm beds with increasing mechanical compaction highly susceptible to porosity reduction and higher velocities
LFS					
CSST	F13–F18	well sorted clastic starvation preserved only in distal settings	little to no bioclastic beds concentration of background fallout micritic carbonate	usually thin laterally extensive cement horizons due to long residence time	overall low porosity, high V_p *proximal:* similar as HST *distal:* low porosity, high V_p
DLS					
HST	F13–F16	coarsening upwards *proximal:* cleaning upwards, accompanied with better sorting *distal:* coarsening upwards without progressive loss of fines, accompanied with decreasing sorting	Low $CaCO_3$ content generally free of bioclastic concentrations	*proximal:* intense bioturbation in combination with lignite-rich sediments leading to tight cementation and/or $CaCO_3$ enrichment *distal:* minor bioturbation; low $CaCO_3$ enrichment	non-uniformly distributed *proximal:* low porosity high V_p *distal:* higher porosity lower V_p with increasing mechanical compaction highly susceptible to porosity reduction and increase in V_p
RSE					
FRWST	F1–F7	coarsening-upwards accompanied with progressive better sorting *proximal:* less large a jump to coarser grain sizes over the RSE *distal:* pronounced jump to coarser grain sizes over the RSE	generally free of bioclastic concentrations	*proximal:* laterally extensive stratabound and concretionary diagenetic $CaCO_3$ enrichment *distal:* laterally extensive stratabound diagenetic $CaCO_3$ enrichment	*proximal:* compartmentalized *distal:* overall low porosity and high V_p, except for the basal bed, directly overlying the RSE
SB					

McGowen 1967) and a depositional systems tract is a linkage of contemporaneous depositional systems (Brown and Fisher 1977). Facies is in this sense a loose unification. Facies associations can be genetically, biologically, or environmentally related. Genetically related facies associations are defined and used in this study as lithofacies. Lithofacies record what is preserved in the stratigraphic record and therefore represent a combination of granulometric facies change, i.e., facies defined by horizontal grain-size gradients, vertical change, i.e., bedding (Swift et al. 2003; Storms and Swift 2003), and biofacies change. Although strongly linked, these two different types of facies need to be separated to allow a physical characterization of processes responsible for the deposition of sediment and the actual physical characterization of specific stacks of sediment (deposits and systems tracts after burial and diagenesis):

Granulometric facies assemblages or associations are produced during the processes of progressive sorting (Russell 1939) and stratal condensation (Crowley 1984), where granulometric facies are differentiated as sediment moves down the pathway in response to transport agents and events (progressive sorting), or when granulometric facies are subjected to

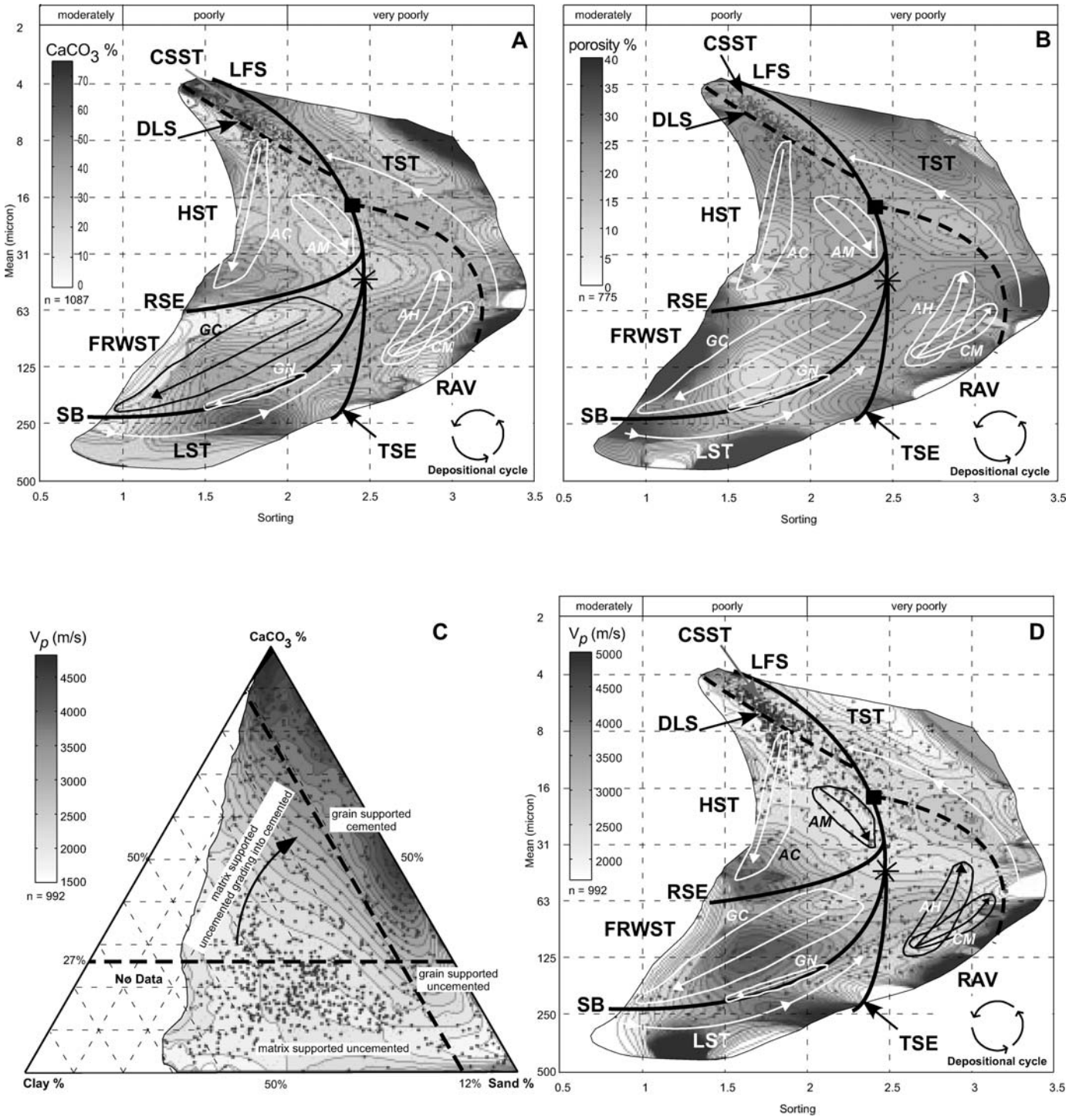

FIG. 9.—Systems tracts: textural, diagenetic, and petrophysical characterization. **A)** Same as in Figure 6A but now overlain by the sequence stratigraphic model as defined in Figure 8A. Elevated $CaCO_3$ content values are intimately related to stratigraphic surfaces but the absolute values depend on the position on a ramp profile where energetic and diagenetic processes are active (see text for discussion). **B)** Same as in Figure 7A but now overlaid by the sequence stratigraphic model as defined in Figure 8A (see text for discussion). **C)** Ternary diagram showing the relationship between P-wave velocity and textural and mineralogical compositions for 992 samples. Indicated are classification boundaries (modified after Braaksma et al. 2003). **D)** Same as in Figure 7B but now overlain by the sequence stratigraphic model as defined in Figure 8A (see text for discussion).

environmental conditions that alter the initial granular composition by means of wave action, currents, scouring, or bioturbation (stratal condensation). Verified on modern shelves (e.g., Snedden and Nummedal 1991), the overall bypassing of fines and the selective deposition of coarser particles in the proximal environments due to a downstream decrease in competence holds for both processes.

Biofacies assemblages are a product of environmental or depositional environment. They comprise the assemblage of bioclasts after death,

decay, and transport (thanatocoenosis) and/or bioturbation (paleoichnocoenoses) but include specific sedimentary structures that provide evidence for environment-specific biological activity. This latter process is usually associated with an increase in precipitation of calcium carbonate cement in sediment subjected to this process, which is also the primary reason why these structures are preserved.

In Figure 5C the volumetric percentage of clay is contoured in the sorting–mean space. Where the mean grain size is most indicative of the position on a ramp profile as a result of the progressive sorting process (Russell 1939; Snedden and Nummedal 1991; Kaufman et al. 1992; Niedoroda et al. 1995; Storms et al. 2002), the sorting of the grain-size distributions records the net result of the progressive sorting, stratal condensation, and biological processes. Overall the data-point distribution in Figure 5C is V-shaped (rotated 90° counterclockwise), and with decreasing mean grain size the volumetric contribution of clay is increasing. However, the contour lines of equal clay percentage are not parallel to the sorting axis. Overall, the relatively fine-grained sediment (interpreted as most distal deposits) and the relatively coarse-grained sediment (interpreted as most proximal deposits) are best sorted, whereas relatively medium-grained sediment (interpreted as deposits at intermediate positions on the sea-floor profile) are most poorly sorted. When cross plotting the mean grain size and the volumetric clay percentage, this relationship becomes even more apparent (Fig. 5D). The gray dashed line shows the best fit through all the data points and the black dashed lines bound the spread around this mean. Where the gray dashed line illustrates the processes of progressive sorting, a significant contribution in the spread of the data points can be related to postdepositional processes like stratal condensation and biological processes. Clay contour lines parallel the skewness and kurtosis contours for coarse bimodal sediment distributions (Fig. 5C). The boundary between bimodal and unimodal and/or polymodal distributions does not coincide with one unique value of clay content. The transition into the bimodal mode can occur with clay contents ranging from 75% (maximum observed value) to 24% (Fig. 5C), indicating that over larger parts of a depositional ramp profile this transition can take place. The most proximal areas, however, consist exclusively of bimodally distributed grain-size distributions.

In Figure 6A the weight percentage of $CaCO_3$ is contoured in the sorting–mean space. As mentioned previously, this percentage is a bulk percentage where no attempt was made to quantitatively distinguish the occurrence of granular, detrital carbonate from chemical, diagenetic carbonate. No apparent relationship between $CaCO_3$ and the mean grain size and sorting is present; elevated values of $CaCO_3$ are scattered throughout the diagram. Bimodal distributions can roughly be divided into three parts. The better-sorted region, containing lower $CaCO_3$ values, occurs on the left side of the diagram, a middle area with elevated $CaCO_3$ values, and a very poorly sorted portion with lower values of $CaCO_3$ on the far right side of the diagram.

Polymodal distributions show the largest variability in $CaCO_3$, and subdivision is not attempted. Bimodal coarse-skewed distributions generally contain little amounts of $CaCO_3$, whereas unimodal distributions show a gradation in $CaCO_3$ from intermediate to high values in carbonate content with decreasing sorting values.

Thus, lithofacies are in essence a combination of the granulometric facies and the biofacies assemblages. Cementation is observed but is not used as a diagnostic parameter in the classification of the lithofacies or their depositional environment. In the Boulonnais study area 18 lithofacies have been identified and ramp position interpreted, principally on the basis of core and outcrop descriptions (Table 1). To convert this descriptive classification into a quantitative classification, facies codes are contoured in the sorting–mean space (Fig. 6B). Increasing facies code numbers, from white to black, indicate more distal environments of deposition. Inner-ramp deposits (lithofacies F1–F7) consist of bimodal grain-size distributions; these distributions are very fine skewed, can be very leptokurtic, leptokurtic, or even mesokurtic, are limited to mean grain-size values of greater than 50 μm, almost cover the entire sorting range, and show a large range in $CaCO_3$ content. Mid-ramp deposits (lithofacies F8–F13) consist mainly of polymodal grain-size distributions, which vary from fine- to coarse-skewed, generally are platy to very platykurtic, have mean grain-size values ranging from 180 to 6 μm, are mainly poorly to very poorly sorted, and show a large range in $CaCO_3$ content. Outer-ramp deposits (lithofacies F14–F18) consist of both unimodal and bimodal grain-size distributions. The deepest (lithofacies F1 and F18) generally are unimodal, whereas the shallower outer-ramp facies generally consist of bimodal distributions. Outer-ramp deposits generally are symmetric or fine-skewed, mesokurtic, and have mean grain sizes varying from 4 to approximately 40 μm. The deepest unimodal outer-ramp deposits have elevated $CaCO_3$ contents, decreasing when shallowing-up, i.e., moving to lower facies codes.

Texture, Mineralogy, and Acoustic Properties

Seismic response and seismic stratigraphic interpretation of reflection data are strongly influenced by the complex relationship between acoustic properties and lithofacies (Vernik and Nur 1992). The seismic sequence stratigraphic concept relies on the basic assumption that stratal surfaces, imaged by seismic reflections, are coincident with depositional surfaces and are essentially time lines (Vail et al. 1977). For time lines to reflect acoustic energy emitted from a source, they must represent acoustic impedance contrasts. Primary control on acoustic impedance is exerted by porosity (Vernik and Nur 1992; Braaksma et al. 2003).

In Figure 7A porosity is contoured in the sorting–mean space. No apparent relationship between porosity and the mean grain size and sorting is present; elevated values of porosity are scattered throughout the diagram. Bimodal distributions show the largest variability in porosity, and subdivision is not attempted. Polymodal distributions show a large variability in porosity as well: a relatively low porous central part, increasing to the outer boundaries, can be observed in this part of the sorting–mean space (Fig. 7A). Bimodal coarse-skewed distributions generally are highly porous, whereas unimodal distributions show a gradation from intermediate to high values in porosity with increasing mean grain-size values. Not unsurprisingly, an apparent relationship between V_p and mean grain size and sorting is not present either (Fig. 7B). Because velocity and porosity are nearly inversely linearly related (Braaksma et al. 2003), areas of high V_p correspond to areas of low porosity in the sorting–mean space (Fig. 7B). Deviations from this inversely related trend can be attributed to the multivariate effects of mineralogy on acoustic properties (Han et al. 1986; Vernik and Nur 1992; Braaksma et al. 2003).

DISCUSSION

The standard sequence stratigraphic model (e.g., Van Wagoner et al. 1988; Posamentier et al. 1988; Fig. 3B) is based mainly on the architecture of sediment accumulations where sea-level fluctuations and sedimentation rates are the two basic forcing factors, but does not directly provide information on rock properties. To quantitatively relate these two important factors to the architecture of deposits on a ramp profile (Figs. 3A, 4), and to quantitatively characterize the physical properties of the systems tracts, the textural and mineralogical changes over and along systems-tracts bounding surfaces need to be quantified. Where sedimentation rate is directly related to the depositional environment (i.e., high proximal and decreasing basinward), the fluctuation of sea level controls the position of depositional environments on the shelf margin and the processes that rework and diagenetically alter initially deposited strata into the present-day observed rock compositions, which ultimately

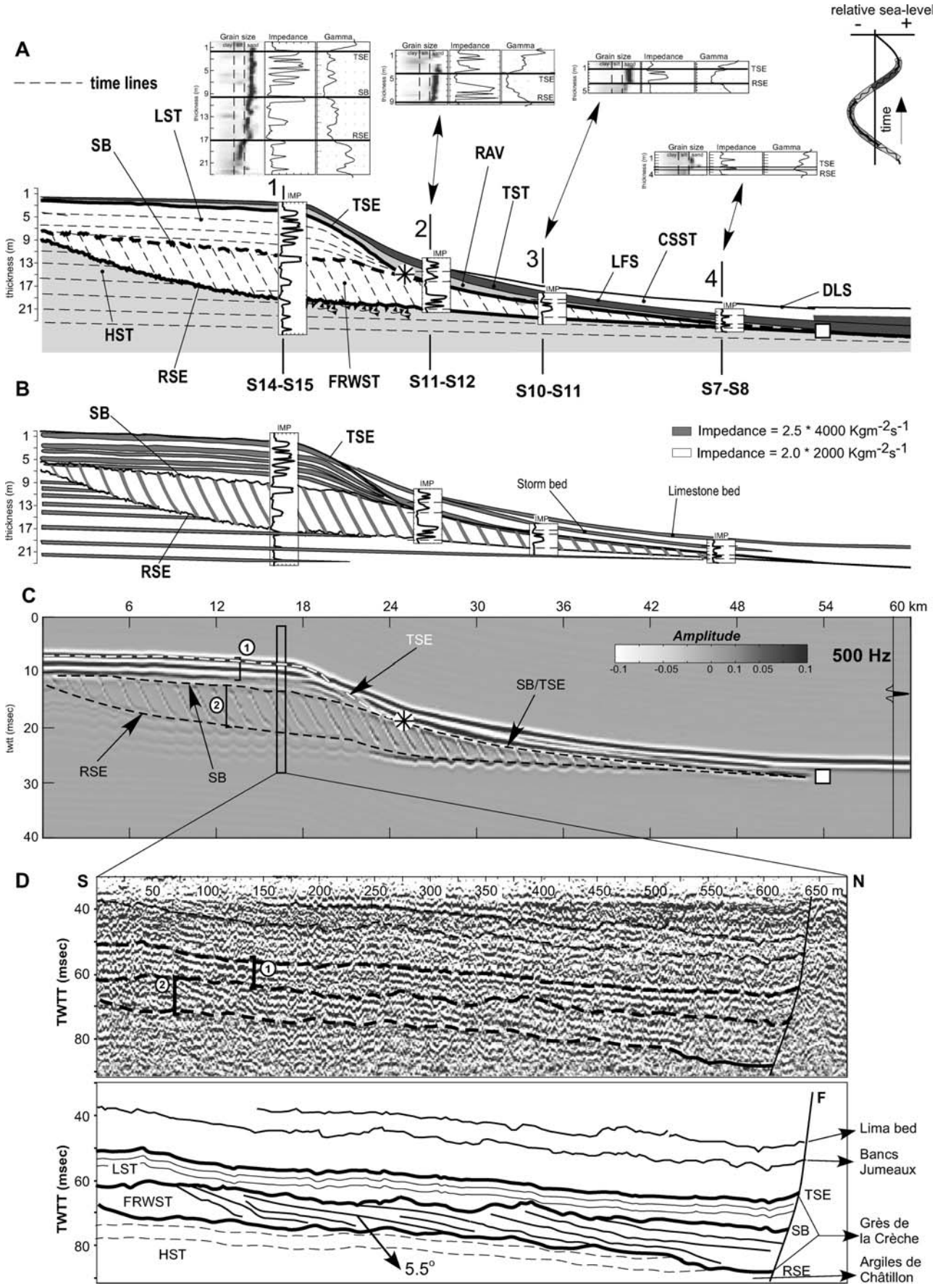
relative sea-level
- +
time
A
time lines
LST
SB
RAV
TST
TSE
CSST
LFS
DLS
HST
RSE
FRWST
S14-S15
S11-S12
S10-S11
S7-S8
Grain size
Impedance
Gamma
clay
silt
sand
thickness (m)
IMP
B
Impedance = 2.5 * 4000 Kgm-2s-1
Impedance = 2.0 * 2000 Kgm-2s-1
Storm bed
Limestone bed
C
Amplitude
500 Hz
SB/TSE
twtt (msec)
D
S
N
TWTT (msec)
F
Lima bed
Bancs Jumeaux
Grès de la Crèche
Argiles de Châtillon
5.5°

determine the physical properties of the systems tracts and therefore observed stratal geometries in seismic reflection profiles.

When possible, grain-size measurements from every sequence that was interpreted at the three section locations (inset Fig. 1B; S1–S18, Figs. 2I, 4) were plotted in the sorting–mean space (Fig. 8A). The key bounding surfaces, separating the different gray shadings and symbols, are indicated with thick black lines. In Figure 8B the same black lines are plotted over the quantified lithofacies distribution in the same sorting–mean space. The quantitative characterization of the systems tracts can be divided into a spatial and a temporal part (Table 3).

Using the various sharp-based shoreface deposits (Grès de Brunembert, S1–S2; Calcaires de Brecquerecques, S7–S8; Grès de Conningthun, S10–S11; Grès de Châtillon, S11–S12; Grès de la Crèche, S14–S15) as (bathymetric) tie points and assuming Walther's law, a spatial characterization of the systems tracts from their more proximal (Grès de la Crèche) to their most distal (Calcaires de Brecquerecques) location with respect to the paleoshoreline (Fig. 3A; Proust et al., 2001) can be made (Figs. 8, 9; Table 3). The granulometric differences in proximal and more distal parts of systems tracts are illustrated by drawing circles around proximal and distal sections of a systems tract (Fig. 8). For example, two different HST coarsening-up, interpreted as shallowing-upward, intervals are indicated in Figure 8A. The HST of S14, corresponding to the upper part of the Argiles de Châtillon Formation (AC11d–AC11e, Figs. 2, 4), as well as the HST of S10, corresponding to the upper part of the Argiles du Moulin Wibert Formation (AM11, Figs. 2, 4), show a coarsening-upward trend. Although both are lignite rich and both contain smectite-dominated clay-mineral associations (Proust et al. 1995), these two data groupings diverge into two different directions, where AC grades up to better-sorted sediment and AM grades up to less-sorted sediment. Comparing the grain-size distributions in the small panels below Figure 8A, the size of the coarser material is larger for AM than for AC and that the fine tail of AM is wider and flatter. Shoaling for AC is accompanied with an upward cleaning (progressive loss of fines leading to lower sorting values) and an increase in the contribution of coarser grains, whereas shoaling for AM is accompanied with an upward shift of the grain-size spectrum as a whole and only minor increase in the contribution of relatively coarse grains, without progressive loss of fines, suggesting a more distal location with respect to the paleoshoreline for AM.

In the temporal characterization of systems tracts, diagenetic processes are addressed. As previously mentioned, bulk $CaCO_3$ content was measured and no quantitative discrimination was made between detrital carbonate and carbonate present as precipitate or cement. However, diagenetic cementation of clastics, with or without detrital carbonate material, is characterized by elevated values of V_p, because cementation leads to framework stiffening and an increase in the effective elastic moduli of an aggregate (Dvorkin and Nur 1998; Mavko et al. 1998). Variations in V_p can, therefore, represent indirect evidence to differentiate the bulk $CaCO_3$ content: in areas of low values in V_p (< 2200 m/s) in Figure 9D, the bulk carbonate measured (Fig. 9A) most likely consists of detrital carbonate rather than carbonate as cement.

Primary control on acoustic velocity (V_p) in the mixed carbonate–siliciclastic rocks in the Boulonnais area is exerted by porosity (V_p decreases with increasing porosity), the remaining variation in V_p can be explained by the opposite and overlapping effect of clay and $CaCO_3$ content (Fig. 9C; Braaksma et al. 2003). Although no clear thresholds defining abrupt changes in physical properties as a function of mineralogical and textural composition are present (Fig. 9C), significant changes in acoustic properties in this data set do overlap, in part, with traditional classification boundaries such as, for example, the change from grain-supported to matrix-supported aggregates (Vernik and Nur 1992) as indicated in Figure 9C. In the sorting–mean space, on the other hand, abrupt changes in physical properties can be observed (Fig. 9B, D).

The physical characteristics of the systems tracts and contrasts in physical properties over and along key bounding surfaces are shown in Figure 9 and are summarized descriptively in Table 3. Combining Figure 9A, B, C, and D, favorable localities of carbonate cement precipitation in these kinds of depositional systems can be inferred and porosity reduction through carbonate cementation as well as acoustic contrasts can now be quantitatively assessed in a sequence stratigraphic framework. This allows predictions of the distribution of physical properties for similar depositional systems and elucidation off diagenetic mechanisms controlling the formation of carbonate cements.

Systems Tracts: Textural, Diagenetic, and Petrophysical Characterization

LST.—The lowstand systems tract (black squares in Fig. 8A) is bounded at its base by a SB (sequence boundary) and at its top by a TSE (transgressive surface of marine erosion) and can be studied in the Grès de la Crèche Formation. The SB separates the FRWST (forced regressive wedge systems tract) from the LST and is indicated by a thick black line in Figure 8A. It can be traced up to the upper data points of the LST, coinciding with the intersection of the TSE (indicated by the black asterisk). The SB does not record well-defined granulometric boundaries between the underlying FRWST and the LST going from proximal to distal locations with respect to the paleoshoreline. The LST shows a decrease in mean grain size with progressive upward deepening accompanied by a shift towards more poorly sorted distributions.

Within the LST, concentration of bioclasts occurs in swash cross-stratified sediment or as single tabular cross-stratified shell gravel beds. In the topmost part of the Grès de la Crèche Formation, below the TSE, spheroidal concretions with diameters up to 5 cm are present. In these, no septarian veins are observed and a diagenetic chemical self-organization process may have controlled the nucleation and growth sites of this kind of concretion, by means of concentrating the available calcite (McBride et al. 2003). The stratigraphic position of these concretions in between the two major flooding surfaces (Figs. 2H, 4) indicates that calcite cementation is promoted by long-term residence in shallow-burial anaerobic diagenetic zones, a condition met beneath flooding surfaces and sequence boundaries, when the depositional rate is low. These low sedimentation rates provide time for the marine shells to dissolve and for the bicarbonate to be precipitated as cement (McBride et al. 2003). The extremely high weight-percentage $CaCO_3$ (up to 70%) suggests that bioclastic material and minor relatively coarse-grained sands must have dominated the initial composition before pronounced diagenesis of the top part (LST) of the Grès de la Crèche Formation. The progradational–aggradational LST shows a gradual increase in $CaCO_3$ content from the base to the top (GC7, 8, and 9 in Fig. 2H). The gradual increase is interrupted only once by an extremely lignite-rich muddy sand layer,

←

FIG. 10.— Geometry, petrophysical characterization, and seismic expression. **A)** Schematic reconstruction of the architecture of a complete Oxfordian–Tithonian sharp-based shoreface deposit and generically related more distally deposited rock volumes, placed in a sequence stratigraphic framework. Section numbers 1–4 correspond to the same sections in Figure 3A. A key for the abbreviations is given in Figure 2 (see text for discussion). **B)** Quantitative impedance model of the reconstructed compound sharp-based shoreface deposit as displayed in Part A (see text for discussion). **C)** Perfectly time-migrated, zero-offset, synthetic seismic time section of Part B using zero-phase Ricker wavelets of 500 Hz as displayed on the far right and the vertical incidence modeling technique. The box shows the dimensions of Figure 11 (see text for discussion).

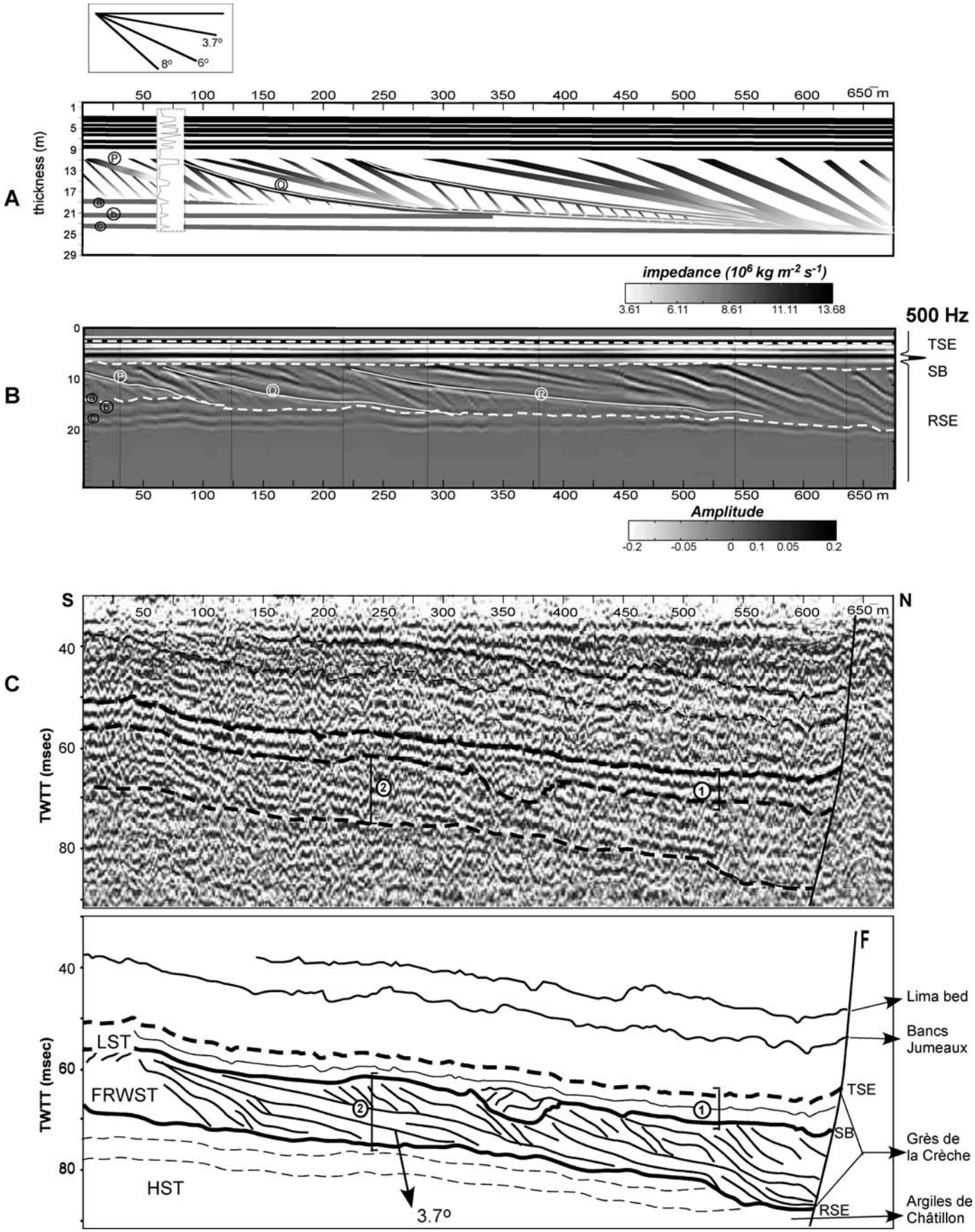
3.7°
8°
6°
A
thickness (m)
impedance (10^6 kg m^{-2} s^{-1})
3.61 6.11 8.61 11.11 13.68
B
500 Hz
TSE
SB
RSE
Amplitude
-0.2 -0.05 0 0.1 0.05 0.2
C
S
N
TWTT (msec)
F
Lima bed
Bancs Jumeaux
LST
FRWST
HST
TSE
SB
RSE
Grès de la Crèche
Argiles de Châtillon
3.7°

embedded in two highly carbonate-cemented muddy sandstone beds (GC7 and 8). The cemented sandstone beds appear as whitened bleached zones in the outcrop and core (corresponding to the Marnes Intercalaires Formation of Proust et al. 1995 and Proust et al. 2001). Similar features have been identified by Taylor et al. (2000) and labeled as "whitecaps." The lateral continuity of these "whitecaps" seems to be directly controlled by the lateral extent of the lignite bed which shows a characteristically higher gamma ray reading than the surrounding sandstones (Figs. 2E, 4).

The LST is porous and characterized by low velocity, uncemented relatively coarse-grained sand beds at its base, but with rising sea level (associated with multiple flooding events), carbonate cementation reduced porosity and increased V_p rapidly at an early diagenetic stage (Fig. 9B, D). Because of lateral variations in mainly the transgressive lowstand facies (overlying parasequence boundaries) containing higher lignite contents, within these tracts porosity and V_p are hard to predict.

TST.—The transgressive systems tract consists of two parts. The ravinement shoreface (RAV) is indicated by gray filled triangles and the TST is indicated by white triangles (Fig. 8A).

Two RAVs are indicated in Figure 8A. AH is overlying the RAV of the Grès de la Crèche Formation (S14–S15, Fig. 4) whereas CM tops the Grès de Conincthun Formation (S14–S15, Fig. 4). Both fine upward, and a small increase in sorting values can be observed where CM is mostly poorly sorted (Fig. 8A). AH and CM are bounded at the base by a TSE. For the CM case this TSE coincides with the SB, because no LST is present. The RAV dominates the lower right part in the sorting–mean space (Fig. 8A). Ravinement shorefaces record multiple flooding events and are identified as a retrogradational stacking of relatively thin parasequences. At parasequence boundaries, concentrations of carbonate bioclasts can occur. At intermediate depositional locations, frequent storm-reworking events led to the concentration of bioclasts.

The ravinement shoreface is thin, generally poorly sorted, and consists of interbedded high (low velocity) and low (high velocity) porosity zones. Proximal ravinement shorefaces, however, are more porous than distal ones. At intermediate positions on the ramp profile the ravinement shoreface is thickest (Fig. 10A) and porosity distribution is highly variable, but because low-porosity beds generally are thin (up to 10 cm), the mean value of porosity for this part of the TST at this position is high (Fig. 9B around the asterisk).

Following the TSE from proximal to distal locations over the ramp profile, $CaCO_3$ values change from low in most proximal areas to high at intermediate areas, to low again at the most distal extent of LST and FRWST sandstones (towards the asterisk in Fig. 9A). The distal continuation of the TSE (the local flooding surface LFS) separates high $CaCO_3$ values from lower ones only in most distal depositional environments (see below). Organic-rich shales usually overlie ravinement shorefaces (Wignall and Newton 2001). Bioclastic concentrations at parasequence boundaries serve as a local source of bicarbonate within these sandy shales, and precipitation of carbonate cement continued through later burial.

A thick dashed line separates the RAV from the TST. The TSE can be traced to the upper data points of the LST (separating black squares from gray triangles) as indicated by the asterisk (Fig. 8A). In these proximal areas, strong erosive and/or reworking processes have led to the formation of the TSE. At intermediate depositional locations, these processes are less pronounced. This area, in between the asterisk and the large black square (Fig. 8A), marks the transition zone between fair-weather and storm-weather wave base (the large black square itself). The remainder of the TSE line is then interpreted as a "normal" marine flooding surface or LFS, separating the TST from the CSST (condensed-section systems tract). The late TST generally contains little $CaCO_3$. Locally high concentrations of $CaCO_3$ in Figure 9A are associated with very poorly sorted, polymodal clastic grain-size distributions, indicating deposition under high-energy conditions, interpreted as bioclastic storm-related event deposits. Bioclastic storm deposits generally are not highly cemented. Possible reasons for this are short residence times, the chemical composition of the bioclastic material, and low permeability, in combination with the isolated nature of these kinds of deposits which prevents extensive, long(er)-term circulation of carbonate-saturated fluids. The TST is thin and shows large variations in porosity (Fig. 9B) and minor variations in velocity (Fig. 9D). Storm-related, very poorly sorted beds may still have high porosity and low V_p, but overall, porosities and velocities are intermediate and low, respectively. Similar to the HST, the porosity and velocity of the TST will most probably decrease and increase, respectively, with increasing burial depths.

CSST.—The condensed-section systems tract (gray dots in Fig. 8A) is bounded at the base by a LFS (local flooding surface) and at its top by a DLS (downlap surface). The CSST consists of unimodal, relatively very fine-grained, well sorted, symmetric, mesokurtic grain-size distributions, and may represent periods of clastic starvation and is developed only in more distal locations on a ramp profile. The bounding DLS (dashed black line in the upper left part of Fig. 8A) can be traced until the most proximal points of the CSST, coinciding with the intersection with the LFS, below storm wave base (Fig. 8A). The distal CSST generally contains no bioclastic material but shows high $CaCO_3$ values. The CSST is located around the turnaround point of sea-level rise and fall. This stillstand is usually marked by lowest clastic sedimentation rates, allowing accumulation of background fallout of relatively very fine-grained (micritic) carbonate material from the water column. The prolonged residence time of sediment on the basin floor favors the diffusive flux of calcium and carbonate ions and the precipitation of carbonate cement (Kantorowicz et al. 1987). The resulting, usually thin, laterally extensive cemented intervals are therefore limited to distal locations. The CSST generally is a low-porosity stratigraphic interval. Where the most distal part is starved of clastic sediment and sedimentation of $CaCO_3$ is dominant, porosity is low and V_p is high. The more proximal CSST shows porosities and velocities similar to those of the late TST and the early HST (Fig. 9B, D).

HST.—A highstand systems tract (black dots in Fig. 8A) is bounded at its base by a DLS (downlap surface and at its top by a RSE (regressive surface of marine erosion). As previously stated, shoaling for AM (S14, Fig. 4) is accompanied by an upward shift of the grain-size spectrum as a whole and only minor increase in the contribution of relatively coarse grains, without progressive loss of fines, suggesting a more distal location with respect to the paleoshoreline for AM than for AC (S10, Fig. 4). Furthermore, comparison of the biofacies of these two HSTs shows that

←

FIG. 11.—Geometry, petrophysical characterization, and seismic expression. **A)** Schemetic reconstruction of the architecture of a proximal section through a sharp-based shoreface deposit. **B)** Perfectly time-migrated, zero-offset synthetic seismic section of Part A using zero-phase Ricker wavelets of 500 Hz. **C)** Offshore 2-D sparker seismic reflection profile located off Wimereux (see Fig. 1 for location) and a line-drawing interpretation below. Peak frequency of the seismic line is approximately 500 Hz. The parallel continuous bundle of high-amplitude reflections (indicated with number 1) is interpreted as the lowstand systems tract part of the composite sharp-based shoreface deposit. The interval indicated with the circle with number two shows progradational geometries (the angle of prograding clinoforms is approximately 3.7°) and is interpreted as the forced regressive systems tract part of the composite sharp-based shoreface deposit (see text for discussion).

AM is more intensely bioturbated than AC. The wider and flatter fine tail of AM is interpreted as a result of burrowing causing sediment mixing in the upper part of the seafloor.

Following the trajectory of the RSE from proximal settings on the far left to intermediate depositional settings (towards the asterisk) a decrease in bulk $CaCO_3$ content can be observed in the upper part of the HST (Fig. 9A). Because no significant bioclastic concentrations are observed in this part of the HST (apart from storm-related shell beds), the elevated $CaCO_3$ content values record diagenetic carbonate enrichment attributed to intense bioturbation in combination with very lignite-rich underlying strata in proximal depositional environments. The carbonate source for this marine cement is interpreted to be the dissolution of detrital carbonate material by organic acids that originate from organic-matter oxidation reactions during early burial, and which were subsequently mobilized by meteoric fluids (Bjørkum and Walderhaug 2003; Taylor et al. 2000; Ketzer et al. 2003; McBride et al. 2003). With increasing water depth and hence decreasing biological diversity and activity in combination with decreasing size and abundance of lignite material, the diagenetic carbonate enrichment decreases. Furthermore, the siliciclastic component of the sediment also becomes less sorted following the trajectory of the RSE, which may very well have reduced permeability and consequently had a pronounced reduction on the circulation of carbonate-saturated fluids, thereby decreasing the cementation potential towards more distal depositional settings. The HST exhibits a nonuniform distribution of porosity and V_p. From proximal to distal locations with respect to the paleoshoreline a slight increase in porosity and a slight decrease in V_p can be observed (Fig. 9B, D). In the HST, along the RSE, a gradation in V_p and porosity can be observed that is similar to the change in carbonate content. Because strata directly overlying the RSE have a low $CaCO_3$ content, are intermediate to highly porous, and have low acoustic velocities, along this surface an acoustic contrast is present only in the more proximal areas. This contrast gradually decreases towards more distal depositional environments on a ramp profile. With increasing burial depths the HST might lose its highly porous character due to mechanical compaction of the predominant shaly lithologies and increasing cementation potential due to organic matter diagenesis, and, consequently, acoustic velocities within the HST may increase.

FRWST.—The FRWST (gray diamonds in Fig. 8A) is bounded at the base by a RSE (regressive surface of marine erosion) and by a SB (sequence boundary) at the top. Two FRWST shallowing-upward intervals are indicated in Figure 8A. GC is the FRWST overlying AC (S14, Fig. 4); GN is the FRWST overlying AM (S10, Fig. 4). Both tracts become better sorted with progressive shoaling, where multiple marine flooding surfaces were observed (Fig. 2F, H). These surfaces clearly indicate that sea-level fall was punctuated by significant multiple higher-frequency sea-level cycles. A more distal location or depositional environment is suggested for the S10 than for S14, because the jump in grain size for sequence S10 (Grès de Connincthun) is large and the transition over the RSE for S14 (Grès de la Crèche) is more gradual (less large a gap between AC and GC data groupings). Going from proximal to distal locations the RSE records a more pronounced contrast in the size of grains. Because no significant bioclastic concentrations are present within the FRWST and there is no apparent difference in the intensity of bioturbation, the elevated $CaCO_3$ content values are interpreted to be diagenetic. During times between the onset of the forced regression and the lowest point of relative sea-level (SB) the freshwater hydraulic head may increase, potentially resulting in ingress of phreatic waters into the underlying FRWST sands, even into more distal sediment packages if permeability was sufficient (Machemer and Hutcheon 1988). Large concretionary carbonate-cemented bodies may be formed by diagenetic dissolution of bioclasts by phreatic waters and reprecipitation of poikilotopic calcite around nuclei (Taylor et al. 1995; Taylor et al. 2000; Ketzer et al. 2003; Al-Ramadan et al. 2004). These concretions are striking features in the outcrops and are present on wave ravinement surfaces on the beaches in the Boulonnais area within the FRWST of the Grès de la Crèche and the Grès de Châtillon formations. Prolonged residence time, punctuation by significant multiple high-frequency sea-level cycles and amalgamation of the TSE and the SB in more distal locations with respect to the paleoshoreline favored the precipitation of $CaCO_3$, which leads to increasing values in V_p. Furthermore, the FRWST is located in between lignite-rich HST sandy shales below and organic-rich mudstones and shales above (best developed distally). Decomposition of this organic matter may have resulted in an increase in carbonate alkalinity and the formation of stratabound calcite cement (Ketzer et al. 2003). The FRWST shows a gradation in porosity from proximal low values to distal high values, as well as vertical compartmentalization by highly cemented, low-porosity, high-V_p sandstone layers (Fig. 2C, D). The basal bed, directly overlying the HST, characteristically remains unaffected by profound cementation over the entire ramp profile, as evidenced by low acoustic velocities (Figs. 2D, 9D).

Geometry, Petrophysical Characterization, and Seismic Expression

The seismic line and cliff sections (including boreholes) are only 5 km apart (Fig. 1B), and the direction of progradation is approximately NE–SW (Proust et al. 2001; Wignall and Newton 2001). Therefore, it is fair to say that a one-to-one comparison between strata observed in outcrop, strata observed through core borings in the intertidal zone, and strata seismically imaged further offshore can be made (Fig. 1B).

Forward seismic modeling of outcrops was introduced 15 years ago and since then has improved the interpretation of reflection seismic data. Particularly successful was the study of lap-out patterns (Rudolph et al. 1989; Biddle et al. 1992; Stafleu and Schlager, 1993; Helland-Hansen et al. 1994; Stafleu 1994; Bracco Gartner 2000). Generally, the construction of synthetic seismic sections of outcrops proceeds according to the following steps: (1) construction of a quantitative lithologic model, (2) determination of the petrophysical properties of the lithologic layers, (3) construction of an impedance model from the lithologic model, and (4) convolution of the impedance model with a seismic wavelet to construct the synthetic seismic section.

The following contrast comparison between outcrop section and borehole-derived synthetic seismic sections and real seismic allows the determination of the origin and nature of the real seismic reflections. From this, it is possible to elucidate depositional setting, paleogeography, and reservoir/aquifer properties from stratal geometries on and from a seismic section. By identifying the key seismic diagnostic criteria for the various systems tracts deposited on a ramp profile, results can be applied to similar shoreface strata and their time-equivalent more distal lithofacies associations that are strongly folded or dissected by faulting.

Construction of a Quantitative Lithologic Model

Shelf physiography affects the rate of regression during sea-level fall significantly. For example, a relative sea-level fall of 10 m, exposing a gently sloping offshore shelf profile with a gradient of 0.02°, results in a seaward shift of the shoreline of 29 km (Posamentier et al. 1992). For this reason an undisturbed (not faulted or folded) outcrop or seismic section showing the lithological expression of a sea-level cycle from the location of the bayline point before relative sea-level fall to the location of the bayline point of the last progradational set before significant flooding and drowning during relative sea-level rise (cf. Fig. 1 of Posamentier et al. 1992) rarely exists for non-recent sedimentary systems, let alone for a complete ramp profile also showing the front of the last prograding clinoform and deposition farther out into the basin.

In the Boulonnais area, from outcrops and boreholes the thickness of a composite sharp-based shoreface deposit is well constrained. Lateral dimensions of, for example, the Grès de la Crèche shoreface deposit, however, can be inferred only from large-scale regional biostratigraphic correlation of outcrops and wells on both sides of the English Channel (Proust et al. 1995; Herbin et al. 1995; Williams et al. 2001; Taylor and Sellwood 2002). An approximate length of an Upper Jurassic ramp profile in the Wessex–Weald Basin of 60 km is inferred from Taylor and Sellwood (2002). An approximate length of the Grès de la Crèche shoreface deposits of 25 km is inferred from Wignall et al. (1996).

Following the geometrical reconstruction (Fig. 3A) proposed by Proust et al. (2001), a plausible scenario for the basin-scale geometry of the Kimmeridgian–Tithonian compound sharp-based shoreface (lithological model) was developed (Fig. 10A). It represents the depositional response of one full sea-level cycle (see Fig. 1B for a tentative location of such a cross section).

Sections belonging to different shoreface deposits are indicated and the sequence numbers (i.e., S14–S15) correspond to the coding used in Figures 2 and 4. For each section grain-size distribution, impedance profile, and gamma-ray counts are displayed. These, along with the vertical thickness of the various sharp-based shoreface deposits, are extracted from the analyses of wire-line logs and cores of VUA-B (Fig. 2). Assuming a constant sediment flux into the basin, the sedimentary response to a sea-level cycle and hence depositional depth can quantitatively be divided into six (physically distinct) parts:

(1) In the HST a gentle sea-level fall is associated with an upward coarsening, where in proximal depositional settings sediments become better sorted and where at more distal depositional locations on a ramp profile sediment become less well sorted. Stratal geometries show low-angle, progradational relationships (dashed lines in Fig. 10A) where in more proximal settings (at Cap Gris Nez) numerous calcite-cemented siltstone ribs and storm-related shell beds are observed, decreasing in abundance in more distally located sections towards the south (Fürsich and Oschmann 1986; Wignall and Newton 2001).

(2) In the FRWST an upwards coarsening and cleaning occurs (better sorting) during an accelerated sea-level fall that is punctuated by significant higher-frequency sea-level oscillations (forced regression). Both mean grain size and sorting reach a minimum value at the turnaround from falling to rising sea level (Fig. 8A). This part of the composite sharp-based shoreface deposit has a thickness of 6.60 m in VUA-B and exhibits well-defined, high-angle downlap patterns (Fig. 10A), which contrast with the low-angle geometrical relationships of the underlying HST (Proust et al. 2001). Associated with the emplacement of these progradational deposits, significant erosive downcutting, during rapid sea-level fall and basinward migration of the shoreline, is demonstrable even at relatively small lateral scales (Fig. 4). This sharp regressive surface of marine erosion is characterized by a marked increase in grain size over major parts of the ramp profile (Fig. 10A).

(3) In the Boulonnais area, the LST is characterized by progressive loss in sorting with slowly rising sea level, accompanied with a less pronounced decrease in mean grain-size (Fig. 8A). The progradational–aggradational geometries within the LST are reconstructed on the basis of field (Schlirf 2003; Wignall et al.1996; Proust et al. 1995) and seismic (Mahieux et al. 1998; Proust et al. 2001) observations. The LST has a thickness of 8.73 m in VUA-B and is characterized by low-angle geometrical relationships in proximal to intermediate depositional settings, which contrasts with the high-angle downlap pattern of the underlying FRWST (Fig. 10A). These two sets of different stratal geometries are separated by an unconformity, which may represent subaerial exposure. This SB, however, cannot be discriminated from other major stratigraphic surfaces over the entire ramp profile. After the point marked with an asterisk it coincides with the TSE (Figs. 8, 9, 10A).

(4) The transgressive surface separating the LST and FRWST from the ravinement shoreface is labeled TSE. The amalgamated SB and TSE can be followed over the ramp profile until the position of the square, past which the strong erosive, cannibalizing activity is reduced significantly and it is labeled LFS (Figs. 8, 9, 10A). The ravinement shoreface may show retrogradational geometries, and at intermediate depositional locations, at the basinward edge of the clinoforms, it has a maximum thickness of 3.10 m in borehole VUA-B and wedges out in both directions (Fig. 10A). The ravinement shoreface deposits are characterized by intermediate gamma-ray counts (Figs. 2D, 10A). During an accelerated rise of relative sea level, shorelines move landward (transgression). Because of reduced sediment influx, one of the principal sources of sediment for transgressive deposits is cannibalization of previously deposited sediment (Arnott 1995). The resulting ravinement shoreface deposits are therefore very poorly sorted, and a slightly fining-upwards trend can be observed from Figure 8A. The reworking of sediment during shoreface retreat (cf. Swift 1975) results in smooth-topped progradational geometries, obliterating any stepwise geometry at the top of sharp-based shoreface deposits at proximal depositional locations.

(5) The late TST shows a retrogradational upward fining, associated with a cleaning-upwards trend (becoming better sorted) where proximal depositional environments are more poorly sorted than distal locations (Fig. 8A). Late TST deposits onlap against the ravinement shoreface deposits (RAV). As previously noted, very poorly sorted, polymodal, bioclastic storm-related event deposits interrupt the overall relatively fine-grained nature of the late TST deposits. At most proximal locations no fining-upwards late TST deposits have been observed (Fig. 2).

(6) Towards the turnaround from rising to falling, unimodal, well sorted, relatively fine-grained sediment of the CSST are deposited. Carbonate-dominated mineralogical associations evidence clastic starvation. The deposition of these fines below storm-weather wave base in most distal parts of the ramp profile result in aggradational geometries.

Construction of the Impedance Model from the Lithologic Model

A quantitative impedance model of the reconstructed compound sharp-based shoreface deposit is displayed in Figure 10B. The petrophysical properties of the lithologic layers have been described above extensively and are summarized in Table 3. Impedance contrasts are mostly concomitant with chronostratigraphic horizons (time lines, Fig. 10A).

Impedance contrasts in the HST are modeled as thin, low-angle layers (0.02°) that represent calcite-cemented siltstone ribs and storm-related shell beds. An impedance value of 10.15×10^6 Kg m^{-2} s^{-1} (4316 m/s * 2.35×10^3 kg/m^3) was assigned to these ribs and beds. The value for V_p is extracted from Figure 9D. The determination of density followed the same procedure as for V_p but is not shown in Figure 9.

Impedance contrasts within the FRWST arise from the calcite-cemented sandstone beds, where each contrast may record one single significant high-frequency sea-level cycle that may have caused a slight steepening of the depositional angle, an increase in residence time, and therefore circumstances favorable for the precipitation of calcium carbonate as cement on the front-side of clinoforms.

On the basis of Figure 9D and the same procedure for density, impedance values for each calcite-cemented sandstone bed decrease from top (13.68×10^6 Kg m^{-2} s^{-1}) to bottom (3.61×10^6 Kg m^{-2} s^{-1}), i.e., from proximal to more distal depositional settings (Fig. 10B). To be able

to show the seismic response over the entire depositional profile but to preserve the downlapping geometries within this systems tract, the angles of these impedance contrasts (here 0.44° vs. 3.7° as expected from Proust et al. 2001) are underestimated in this model (see angles inset in Fig. 10A, B). For the same reason, not all impedance contrasts at the scale of observations from cliff and boreholes (Figs. 2, 3, 4) have been included.

Impedance contrasts within the LST are modeled as retrogradational, laterally continuous layers that are truncated at intermediate depositional locations (around 20 km) by the TSE (Fig. 10B). LST sandstone beds toplap the FRWST sands (sandstones), where the unconformity is classified as a SB. On the basis of Figure 9D and the same procedure for density, the highly cemented sandstone beds have an average impedance value of 13.68×10^6 Kg m^{-2} s^{-1}.

Within the ravinement shoreface an impedance contrast is modeled at the base and from Figure 9D and the same procedure for density; an average impedance value of 10.15×10^6 Kg m^{-2} s^{-1} is inferred. This bed wedges out in both directions (Fig. 10B; S11–S12).

Within the TST an impedance contrast is modeled at the top and represents a storm-related shell bed deposited on a LFS. This bed onlaps the ravinement shoreface and the distal part of the LST at intermediate depositional locations and the HST at most distally locations. On the basis of Figure 9D and the same procedure for density, an average impedance value of 9.21×10^6 Kg m^{-2} s^{-1} (4012 m/s * 2.29×10^3 kg/m^3) was assigned for this bed.

The uppermost impedance contrast in Figure 10B represents a micritic limestone bed deposited at the turnaround point of sea level rise and fall when clastic sedimentation rates are lowest. This bed onlaps the TST at intermediate locations on the ramp profile. On the basis of Figure 9D and the same procedure for density, this bed shows an increase in V_p (and density) from proximal to distal locations. Therefore, this bed is modeled with impedance values of 10.15×10^6 Kg m^{-2} s^{-1} at around 27 km increasing to 13.68×10^6 Kg m^{-2} s^{-1} at most distal locations. To the areas displayed without any color (white), a background impedance value of 3.61×10^6 Kg m^{-2} s^{-1} (1900 m/s * 1.9×10^3 kg/m^3) was assigned.

For a contrast comparison with real seismic data, a second impedance model was constructed analogous to the procedure mentioned above and impedance values for different units (Fig. 11A) shown at the same horizontal scale as the real seismic section. Borehole VUA-B was used as a tie point. To display the reconstructed internal configuration of this relatively proximal part of the FRWST properly, the vertical scale has been exaggerated (see inset Fig. 11A). In the impedance model, foreset angles increase from the first downstepping surface (P, Q, and R in Fig. 11) with depositional time. This steepening of angles can be attributed to high-frequency slower sea-level rises after relatively rapid sea-level falls superimposed on an overall sea-level fall (e.g., Kolla et al. 2000). For illustrative purposes no more steeply inclined (small) foresets have been included in the most distal part of the model.

Convolution of the Impedance Models with Seismic Wavelets

The models (Fig. 10B) were convolved with a 500 Hz zero-phase Ricker wavelet. By using the vertical-incidence technique, the resulting synthetic seismic section (Figs. 10C, 11B) are perfectly migrated, zero-offset time sections, where each trace (270 in total for each section) is equivalent to a one-dimensional seismogram of an imaginary borehole at each trace location. Amplitudes are relative and the gain was kept equal for each trace.

Using this high a frequency, the synthetic seismic sections clearly resemble the impedance models (Figs. 10, 11). Comparing the synthetic seismic section of 11B with a part of the seismic line (Bdb95004), shot offshore Wimereux under rough-weather conditions (see Fig. 1B for location), the key diagnostic criteria for sharp-based shoreface deposits in a quantitative sequence stratigraphic framework can be identified:

The low-angle-dipping ribs within the HST are seismically resolved but appear ringy in the seismic section because of the modeling technique used (Fig. 10C). They can still be followed from proximal to distal depositional environments as high(er)-amplitude positive reflections.

The RSE is seismically expressed as a discontinuous reflector because on the RSE more steeply inclined downlapping FRWST beds (along with "retrogradational" diagenetic enhancement of frontal parts of clinoforms) truncate lower-inclination, higher-impedance highstand systems tract (HST) storm-related beds (Fig. 11A, B, C). Because most of the sandy lithofacies that are deposited directly on the RSE remain unaffected by pronounced cementation (Fig. 9), only in cases when the RSE truncates HST-storm beds positive reflection coefficients occur and positive amplitude reflections may be recorded. When high-impedance clinoform fronts approach higher-impedance HST-storm beds it depends on the inclination of the first and the incident frequency of the acoustic wave whether a reflection occurs (Fig. 11B). Negative amplitudes along the RSE occur when clinoform fronts approach low-impedance HST intervals (Fig. 11B). RSEs show an overall convex-down pattern, which finds its origin in the downcutting of forestepping sets of higher-order sandy sequences into relatively finer-grained HST deposits during relative sea-level fall. These downstepping geometries are, however, poorly resolved at the scale of the real seismic section. RSEs may also show a change in geometry at intermediate depositional locations (at the point indicated with an asterisk in Fig. 11). This point marks the transition where the updip unconformity goes over in a downdip conformity.

The FRWST is characterized by the most steeply inclined reflections that downlap on the RSE (Figs. 10, 11). From close examination of impedance contrast in this interval on core and logs, these reflections are interpreted to represent fronts of migrating sequences, which have been truncated by a transgressive surface of marine erosion during significant amplitude, high-frequency sea-level oscillations superimposed on an overall sea-level fall. These higher-amplitude positive reflections within the FRWST can be regarded as one of the diagnostically most important features of sharp-based shoreface deposits. When using a coarse lateral sampling (shotpoint interval), these clinoforms have a checkered appearance (Fig. 10C).

Fronts of clinoforms that downlap on the RSE are truncated at proximal depositional locations by a sequence boundary (SB). During the maximum lowstand, deep(er) erosion related to the development of an incised-valley system may occur across the top of the prograding wedges (Fig. 11C). This unconformity modifies all of the previous updip RSE and clinoform front unconformities. Infilling of the incised-valley system occurs mainly during the early rise of sea level. In the Boulonnais area, these kinds of deposits (the Marnes Intercalaires Formation; Fig. 4) are typified by concentration of terrestrial debris in a muddy coarse-grained sand matrix. Even at the scale of the paleogeographic reconstruction, this interval is discontinuous: it pinches out towards the north and thins towards the south (Fig. 4). In 11C, it is characterized by a chaotic, landward-dipping reflection pattern, although at some locations it appears transparent as well (Fig. 11C).

On the SB, reflectivity is caused by high-impedance frontal parts of clinoforms and overlying unconsolidated muddy sandstones. In proximal to intermediate depositional environments, the seismic expression of the SB is therefore just as discontinuous as for the RSE because pronounced cementation, and hence high-impedance values, generally do not affect basal parts of channel fills (Fig. 9). However, in both the synthetic sections and the real seismic data the SB appears as a continuous but variable amplitude positive reflection, and can be marked as a seismic artifact.

The upper part of the LST records a retrogradational development of the shoreface. In borehole VUA-B, shoreface retreat (cf. Swift 1975) and reduction of siliciclastic flux input is evidenced by an overall gradual increase of standardized weight percentage $CaCO_3$. This last phase of

early sea-level rise is seismically expressed as a bundle of gently seaward-dipping, parallel reflections that toplap the FRWST (Figs. 10, 11).

At approximately the same time as LST development, an onlapping "healing-phase" wedge develops in deeper-water settings (Kolla et al. 2000). Because this interval is generally poorly preserved, it is continuously reworked with ongoing sea-level rise and cannot be quantitatively discriminated from a ravinement shoreface (RAV), the most logical location to place the transgressive surface of marine erosion is at the base of a healing-phase wedge. As a consequence, only in more proximal depositional settings LSTs are sediments interpreted in between the SB and the TSE. At intermediate to distal locations the SB and TSE coincide (Fig. 10). Because of reduced sediment influx with ongoing sea-level rise, one of the principal sources of sediment for transgressive deposits is cannibalization of previously deposited sediment. This process is strongest at the delta front. Therefore, the resulting ravinement shoreface (RAV) deposits develop thickest at the toe of FRWST and LST slopes (Fig. 10A).

At more proximal depositional locations (0–18 km), landward of the shelf-break, the ramp profile experienced siliciclastic sediment starvation during relative but accelerated sea-level rise. Coarse-grained and poorly sorted uncemented sands characterize the very thin RAV observed at the top of the Grès de la Crèche Formation (AH1; Fig. 2H). The extremely large difference in impedance values of the uppermost part of the LST and the RAV results in step-like impedance contrasts, and hence high-amplitude positive reflections in proximal to intermediate depositional settings characterize the TSE (Figs. 10, 11). At intermediate to distal depositional locations (19–33 km, Fig. 10), closely spaced impedance contrasts within the RAV (modeled as one thicker bed) are constructively tuned and abnormally high positive amplitude reflections generally result. Because in these settings the TSE comprises the basal contact with unconsolidated FRWST sands, strong negative amplitudes characterize it. Between 18 and 19 km (Fig. 10), a 180 degree phase shift should occur along the trajectory of the TSE. This phase shift could not be resolved at this scale and in these depositional settings the TSE cannot be followed continuously (Fig. 10C). The remainder of the RAV and the early part of the late TST is characterized by a seismically transparent interval (thickest around 28 km) bounded at the top by high impedance, resulting in a high-amplitude-positive-reflection TST storm bed (Fig. 10C).

The CSST is characterized by a high-amplitude positive reflection. Where the high impedance bed within the CSST onlaps the TST shellbed (at approx. 30 km), the last is destructively tuned with the first. A chronostratigraphical identification of seismic horizons should therefore follow not the uppermost reflection at this point but the one directly below. Over major parts of the ramp profile (30–48.5 km) the TST and CSST beds are imaged as three reflectors, where the last can be identified as a seismic artifact caused by constructive tuning of the real impedance contrasts. This is evidenced at locations from 51 km onwards. Basinwards from this point, no impedance contrast is present in the model (Fig. 10B); nevertheless, a high-amplitude reflection, originating from the overlying limestone bed, can be observed at approximately the same time the reflection of the storm bed would have continued if it had been included in the impedance model (Fig. 10C).

CONCLUSIONS

The high sampling resolution of granulometric and mineralogic data from core borings and outcrop in the Late Jurassic shoreface-dominated shelf margin in northern France provided the basis for a conversion of classic descriptive observations into quantitative physical stratigraphic determinations to be able to quantitatively interpret a reflection seismic image shot over the same stack of sequences. The primary results are the following:

(1) High-quality continuous cores of the Tithonian through Oxfordian strata for the first time allows a detailed correlation and sequence stratigraphic interpretation between basinal sections in England and marginal sections in the Boulonnais for the complete Kimmeridgian section.

(2) Geostatistical analysis of granulometric facies and bulk carbonate content provides a physical quantification of depositional environments, systems tracts, and their key bounding surfaces across the complete depositional profile. This provides important insights into lateral continuity of petrophysical and geochemical parameters above and below these surfaces.

(3) Acoustic properties are controlled by porosity, and the remaining variation can be explained by the opposite and overlapping effects of clay and carbonate content. Carbonate cement precipitation is the principal diagenetic process. Intensity and abundance of carbonate cementation is generally stratabound and is assessed quantitatively in a sequence stratigraphic framework. These results can therefore be used as input for numerical stratigraphic forward models to assign more reliable acoustic properties to sedimentary bodies, allowing them to be directly applicable to seismic stratigraphic analyses.

(4) By synthetic seismic modeling of the sedimentary and petrophysical response of a full depositional cycle over a complete ramp profile, diagnostic stratal geometries observed in seismic sections of similar depositional systems can be tied to a their specific depositional environment and hence predictions on reservoir/aquifer properties and dimensions outside the grid of a seismic survey can be made. These include for proximal depositional settings:

Concave-down and erosional downstepping geometries below a bundle of parallel-aggradational lowstand systems tract reflections; a clear angular relationship between inclined forced regressive wedge clinoforms and relatively flat-lying lowstand and highstand systems tract reflectors; increasing angles of reflectors in a seaward direction within the forced regressive systems tract; the presence of a seismic transparent interval or landward-dipping, laterally small reflections in otherwise seaward dipping reflectors.

These include for intermediate depositional settings: more steeply seaward-dipping laterally confined above-normal amplitude reflections originating from the ravinement shoreface; onlap and lateral phase shifts (up to 180°) and erosional downstepping geometries.

These include for distal depositional settings: parallel-aggradational reflections and above-normal amplitudes due to constructive interference of relatively thin impedance contrasts.

(5) The physical model presented in this paper allows ground-truthing of sequence stratigraphic principles. Through a contrast comparison with synthetic seismic sections of this model and a real seismic line shot over exactly the same sequence, it shows that some key bounding surfaces are in fact discontinuous seismic reflections.

ACKNOWLEDGMENTS

We thank Bruis Gianotten for his help with the data acquisition in France and for his help in the petrophysics laboratory at the Vrije Universiteit in Amsterdam. We thank Martin Konert for constructive advice and help in the grain-size analysis. We would also like to thank TOTAL for funding the drilling of VUA-A, EGS (Luxembourg) for providing logging services, and Geoffroy Mahieux for assisting in the core handling and logistics. Marc DeBatist and colleagues of RCMG, Gent are acknowledged for the acquisition of, and their kindness to use the Bdb95004 seismic line in this paper.

REFERENCES

Ager, D.V., and Wallace, P., 1966, The environmental history of the Boulonnais; France: Proceedings of the Geological Association, v. 77, p. 385–417.

Ahr, W.M., 1973, The carbonate ramp: an alternative of the shelf model: Gulf Coast Association of Geological Societies, Transactions, v. 23, p. 221–225.

Aigner, T., 1985. Storm Depositional Systems: Berlin, Springer-Verlag, Lecture Notes in Earth Sciences 3, 174 p.

Al-Ramadan, K., Morad, S., Eklund, S., and Proust, J.N., 2004. Calcite cementation patterns and textural habits within sequence stratigraphic framework of Upper Jurassic siliciclastic successions, Boulonnais, France, 26th Nordic Geological Winter Meeting, January 6–9 2004, Uppsala, Sweden,

Arnot, R.W.C., 1995, The parasequence definition—are transgressive deposits inadequately addressed?: Journal of Sedimentary Research, v. 65, p. 1–6.

Baum, G.R., and Vail, P.R., 1988, Sequence stratigraphic concepts applied to Paleogene outcrops, Gulf and Atlantic Basins, *in* Wilgus, C.K., Hastings, B.S., Kendall, C.G.St.C., Posamentier, H.W., Ross, C.A., and Van Wagoner, J.C., eds., Sea-level Changes—An Integrated Approach: SEPM, Special Publication 42, p. 309–327.

Biddle, K.T., Schlager, W., Rudolph, K.W., and Bush, T.L., 1992, Seismic model of a progradational carbonate platform, Picco di Vallandro, the Dolomites, northern Italy: American Association of Petroleum Geologists, Bulletin, v. 76, p. 14–30.

Bjørkum, P.A., and Walderhaug, A., 2003, Geometric arrangement of calcite cementation within shallow marine sandstones: Earth-Science Reviews, v. 29, p. 145–161.

Blott, J.S., and Pye, K., 2001, Gradistat: A grain size distribution and statistics package for the analysis of unconsolidated sediments: Earth Surface Processes and Landforms, v. 26, p. 1237–1248.

Braaksma, H., Kenter, J.A.M., Proust, J.N., Dijkmans, V., van Hoek, T., Mahieux, G., and Drijkoningen, G.G., 2003, Controls on acoustic properties of Upper Jurassic siliciclastic rocks (Boulonnais, northern France): Geophysics, v. 68, p. 58–69.

Bracco Gartner, G.L., 2000. High resolution impedance models of outcrops and their application in seismic interpretation [Ph.D. Thesis]: Vrije Universiteit Amsterdam, ISBN: 90-9013666-5.

Brown, R.E., and Fisher, W.L., 1977, Seismic stratigraphic interpretation of depositional surfaces: examples from Brazilian rift and pull-apart basins, *in* Payton, C.E., ed., Seismic Stratigraphy—Applications to Hydrocarbon Exploration: American Association of Petroleum Geologists, Memoir 26, p. 213–248.

Bruun, P., 1962, Sea-level rise as a cause of shore erosion: American Society of Civil Engineering, Proceedings, Journal of the Water and Harbour Division, v. 88, p. 117–130.

Burchette, T., and Wright, V., 1992, Carbonate ramp depositional systems: Sedimentary Geology, v. 79, p. 3–57.

Carmichael, R.S., 1990. Practical Handbook of Physical Properties and Minerals: Boca Raton, Florida, U.S.A., CRC Press, 741 p.

Carter, M.R., Fulthorpe, C.S., and Naish, T.R., 1998, Sequence concepts at seismic and outcrop scale: the distinction between physical and conceptual stratigraphic surfaces: Sedimentary Geology, v. 122, p. 165–179.

Crowley, K.D., 1984, Filtering of depositional events and the completeness of the sedimentary record: Journal of Sedimentary Petrology, v. 54, p. 127–136.

Dvorkin, J., and Nur, A., 1998, Time-average equation revisited: Short Note: Geophysics, v. 63, p. 460–464.

Einsele, G., 1985, Response of sediments to sea-level changes in differing subsiding storm-dominated marginal and epeiric basins, *in* Bayer, U., and Seilacher, A., eds., Sedimentary and Evolutionary Cycles: Springer: Berlin, p. 68–97.

El Albani, A., Deconinck, J.F., Herbin, J.P., and Proust, J.N., 1993, Caractérisation géochimique de la matière organique et minéralogie des argiles du Kimméridgien du Boulonnais: Annales de la Societé Géologique du Nord, v. 2, p. 113–120.

Fisher, W.L., and McGowen, J., 1967, Depositional systems in the Wilcox Group of Texas and their relationship to the occurrence of oil and gas: Gulf Coast Association of Geological Societies, v. 17, p. 105–125.

Flemings, P.B., and Grotzinger, J.P., 1996, STRATA:freeware for analyzing classic stratigraphic problems, GSA Today, v. 6, p. 1–7.

Flügel, E., 1982. Microfacies Analysis of Limestones: Berlin, Springer-Verlag, 633 p.

Friedman, G.M., and Johnson, K.G., 1982. Exercises in Sedimentology: New York, Wiley, 208 p.

Fürsich, F.T., and Oschmann, W., 1986, Storm shell beds of *Nanogyra virgula* in the Upper Jurassic of France: Neues Jahrbuch für Mineralogie, Geologie und Paläontologie, Abhandlungen, v. 172, p. 141–161.

Gallois, R.W., 2000, The stratigraphy of the Kimmeridge Clay Formation (Upper Jurassic) in the RGGE Project boreholes at Swanworth Quarry and Metherhills, south Dorset: Proceeding of the Geological Association, v. 111, p. 265–280.

Gallois, R.W., and Cox, B.M., 1976, The stratigraphy of the Lower Kimmeridge Clay of eastern England: Yorks Geological Society, Proceedings, v. 41, p. 13–26.

Guillocheau, F., 1990. Stratigraphie séquentielle des bassins de plateforme: l'exemple dévonien armoricain [Thèse de Doctorat es Sciences]: Université Louis Pasteur: Strasbourg, France, 257 p.

Han, D.-H., Nur, A., and Morgan, D., 1986, Effects of porosity and clay content on wave velocities in sandstones: Geophysics, v. 51, p. 2093–2107.

Helland-Hansen, W., Helle, H.B., and Sunde, K., 1994, Seismic modelling of Tertiary sandstone clinothems, Spitsbergen: Basin Research, v. 6, p. 181–191.

Herbin, J.P., Fernandez-Martinez, J.L., Geyssant, J.R., El Albani, A., Deconinck, J.F., Proust, J.N., Colbeaux, J.P., and Vidier, J.P., 1995, Sequence stratigraphy of source rocks applied to the study of the Kimméridgian/Tithonian in the north-west European shelf (Dorset, U.K., Yorkshire, U.K. and Boulonnais, France): Marine and Petroleum Geology, v. 12, p. 177–194.

Hunt, D., and Tucker, M.E., 1992, Stranded parasequences and the forced regressive wedge systems tract: deposition during base-level fall: Sedimentary Geology, v. 81, p. 1–9.

Hunt, D., and Tucker, M.E., 1995, Stranded parasequences and the forced regressive wedge systems tract: deposition during base-level fall—reply: Sedimentary Geology, v. 95, p. 147–160.

Kantorowicz, J.D., Bryant, I.D., and Dawans, J.M., 1987, Controls on the geometry and distribution of carbonate cements in Jurassic sandstones: Bridport Sands, southern England and Viking Group, Troll Field, Norway, *in* Marshall, J.D., ed., Diagenesis of Sedimentary Sequences: Geological Society of London, Special Publication 36, p. 103–118.

Kaufmann, P., Grotzinger, J.P., and McCormick, D.S., 1992, Depth-dependent diffusion algorithms for simulation of sedimentation in shallow marine depositional systems, *in* Franseen, E.K., Watney, W.L., Kendall, C.G.St.C., and Ross, W., eds., Sedimentary Modeling: Computer Simulations and Methods for Improved Parameter Definition: Kansas Geological Survey, Special Publication 233, p. 489–508.

Kenter, J.A.M., and Ivanov, M., 1995, Parameters controlling acoustic properties of carbonate and volcaniclastic sediments at sites 866 and 869, *in* Winterer, E.L., Sager, W.W., and Sinton, J.M., eds., Proceedings of the Ocean Drilling Program, Scientific Results, v. 143, p. 305–316.

Kenter, J.A.M., Podladchikov, F.F., Reinders, M., Van der Gaast, S.J., Fouke, B.W., and Sonnenfeld, M.D., 1997, Parameters controlling sonic velocities in a mixed carbonate–siliciclastics Permian shelf-margin (upper San Andres Formation, Last Chance Canyon, New Mexico): Geophysics, v. 62, p. 505–520.

Ketzer, J.M., Holz, M., Morad, S., and Al-Aasm, I.S., 2003, Sequence stratigraphic distribution of diagenetic alterations in coal-bearing, paralic sandstones: evidence from the Rio Bonito Formation (Early Permian), southern Brazil: Sedimentology, v. 50, p. 855–877.

Kolla, V., Biondi, P., Long, B., and Fillon, R., 2000, Sequence stratigraphy and architecture of the late Pleistocene Lagniappe delta complex, northeast Gulf of Mexico, *in* Hunt, D., and Gawthorpe, R.L., eds., Sedimentary Responses to Forced Regression: Geological Society of London, Special Publication 172, p. 291–327.

Konert, M., and Vandenberghe, J., 1997, Comparison of laser grain size analysis with pipette and sieve analysis: a solution for underestimation of the clay fraction: Sedimentology, v. 44, p. 523–535.

Krumbein, W.C., and Pettijohn, F.J., 1938. Manual of Sedimentary Petrography: New York, Appleton-Century-Crofts, 549 p.

Loizeau, J.L., Arbouille, D., Santiago, S., and Vernet, J.P., 1994, Evaluation of a wide range laser diffraction grain size analyzer for use with sediments: Sedimentology, v. 41, p. 353–361.

Machemer, S.D., and Hutcheon, I., 1988, Geochemistry of early carbonate cements in the Cardium Formation, central Alberta: Journal of Sedimentary Petrology, v. 58, p. 136–147.

Mahieux, G., Proust, J.N., Tessier, B., and Debatist, M., 1998, Comparison between high-resolution seismic and sequence stratigraphic approaches applied to the Upper Jurassic deposits of the Dover strait area (Northern France): Marine and Petroleum Geology, v. 15, p. 329–342.

Mavko, G., Mukerji, T., and Dvorkin, J., 1998. The Rock Physics Handbook; Tools for Seismic Analysis of Porous Media: Cambridge, U.K., Cambridge University Press, 329 p.

McBride, E.F., Picard, M.D., and Milliken, K.L., 2003, Calcite-cemented concretions in Cretaceous sandstone, Wyoming and Utah, U.S.A.: Journal of Sedimentary Research, v. 73, p. 462–483.

McCave, I.N., Bryant, R.J., Cook, H.F., and Coughanowr, C.A., 1986, Evaluation of a laser diffraction size analyzer for use with natural sediments: Journal of Sedimentary Petrology, v. 56, p. 561–564.

Mitchum, R.M., Vail, P.R., and Thompson, S, Iii, 1977, Seismic stratigraphy and global changes of sea level, Part 2: The depositional sequence as a basic unit for stratigraphic analysis, *in* Payton, C.E., ed., Seismic stratigraphy—applications to hydrocarbon exploration: American Association of Petroleum Geologists, Memoir 26, p. 53–62.

Niedoroda, A.W., Reed, C.W., Swift, D.J.P., Arato, H., and Hoyanagi, K., 1995, Modeling shore-normal large-scale coastal evolution: Marine Geology, v. 126, p. 181–199.

Oschmann, W., 1990, Environmental cycles in the Late Jurassic northwest European epeiric basin: interaction with atmospheric and hydrospheric circulations: Sedimentary Geology, v. 69, p. 313–332.

Overeem, I., Veldkamp, A., Tebbens, L., and Kroonenberg, S.B., 2003, Modelling Holocene stratigraphy and depocentre migration of the Volga delta due to Caspian Sea-level change: Sedimentary Geology, v. 159, p. 159–175.

Posamentier, H.W., and Vail, P.R., 1988, Eustatic controls on clastic deposition II. Sequence and systems tract models, *in* Wilgus, C.K., Hastings, B.S., Kendall, C.G.St.C., Posamentier, H.W., Ross, C.A., and Van Wagoner, J.C., eds., Sea-level Changes—An Integrated Approach: SEPM, Special Publication 42, p. 125–154.

Posamentier, H.W., Jervey, M.T., and Vail, P.R., 1988, Eustatic controls on clastic deposition I. Conceptual framework, *in* Wilgus, C.K., Hastings, B.S., Kendall, C.G.St.C., Posamentier, H.W., Ross, C.A., and Van Wagoner, J.C., eds., Sea-level Changes—An Integrated Approach: SEPM, Special Publication 42, p. 109–124.

Posamentier, H.W., Allen, G.P., James, D.P., and Tesson, M., 1992, Forced regressions in a sequence stratigraphic framework: concepts, examples, and exploration significance: American Association of Petroleum Geologists, Bulletin, v. 76, p. 1687–1709.

Prothero, D.R., and Schwab, F., 1996. Sedimentary Geology; An Introduction to Sedimentary Rocks and Stratigraphy: New York, W.H. Freeman and Company, 85 p.

Proust, J.N., Deconinck, J.F., Geyssant, J.R., Herbin, J.P., and Vidier, J.P., 1993, Nouvelles données sédimentologiques dans le Kimmeridgien et le Tithonien du Boulonnais (France): Academié des Sciences, Paris, v. 316, p. 363–369.

Proust, J.N., Deconinck, J.F., Geyssant, J.R., Herbin, J.P., and Vidier, J.P., 1995, Sequence analytical approach to the Upper Kimmeridgian–Lower Tithonian storm-dominated ramp deposits of the Boulonnais (Northern France). A landward time equivalent to offshore marine source rocks: Geologische Rundschau, v. 84, p. 255–271.

Proust, J.N., Mahieux, G., and Tessier, B., 2001, Field and seismic images of sharp-based shoreface deposits: Implications of sequence stratigraphic analysis: Journal of Sedimentary Research, v. 71, p. 944–957.

Read, J.F., 1985, Carbonate platform facies model. American Association of Petroleum Geologists, Bulletin, v. 69, p. 1–21.

Rudolph, K.W., Schlager, W., and Biddle, K.T., 1989, Seismic models of carbonate foreslope-to-basin transition, Picco di Vallandro, Dolomite Alps, northern Italy: Geology, v. 17, p. 453–456.

Russell, R.D., 1939, Effects of transportation on sedimentary particles, *in* Trask, P.D., ed., Recent Marine Sediments: American Association of Petroleum Geologists, Bulletin, p. 32–47.

Schlirf, M., 2003, Palaeoecologic significance of Late Jurassic trace fossils from the Boulonnais, N. France: Acta Geologica Polonica, v. 53, p. 123–142.

Seilacher, A., 1984, Constructional morphology of bivalves: evolutionary pathways in primary versus secondary soft-bottom dwellers: Paleontology, v. 27, p. 207–237.

Schnyder, J., Baudin, F., Deconinck, J.F., Durlet, C., Jan du Chene, R., and Lathuiliere, B., 2001, Stratigraphie et analyse sédimentologique du passage Oxfordien/Kimméridgien dans le Boulonnais: Géologie de la France, v. 4, p. 21–37.

Snedden, J.W., and Nummedal, D., 1991, Origin and geometry of storm-deposited sand beds in the modern sediments of the Texas continental shelf, *in* Swift, D.J.P., Oertel, G.F., Tillman, R.W., and Thorne, J.A., eds., Shelf Sand and Sandstone Bodies: International Association of Sedimentologists, Special Publication 14, p. 283–308.

Stafleu, J., 1994. Seismic models of outcrops as an aid in seismic interpretation [Ph.D. Thesis]: VrijeUniversiteit: Amsterdam, ISBN: 90-9007601-8.

Stafleu, J., and Schlager, W., 1993, Pseudo-toplap in seismic models of the Schlern–Raibl contact (Sella platform, northern Italy): Basin Research, v. 5, p. 55–65.

Stafleu, J., and Sonnenfeld, M.D., 1994, Seismic models of a shelf margin depositional sequence: upper San Andres Formation, Last Chance Canyon, New Mexico: Journal of Sedimentary Research, v. 64, p. 481–499.

Steckler, M., 1999, High-resolution sequence stratigraphic modeling 1: The interplay of sedimentation, erosion, and subsidence, *in* Harbaugh, J.W., Watney, W.L., Rankey, E.C., Slingerland, R., Goldstein, R.H., and Franseen, E.K., eds., Numerical experiments in Stratigraphy: Recent advances in Stratigraphic and Sedimentologic Computer Simulations: SEPM, Special Publication 62, p. 139–149.

Stenzel, H.B., 1971, Oysters, *in* Moore, R.C., and Teichert, C., eds., Treatise on Invertebrate paleontology (N) Mollusca 6, Bivalvia: Geological Society of America, and University of Kansas: Lawrence, Kansas, U.S.A., p. 953–1224.

Storms, J.E.A., and Swift, D.J.P., 2003, Shallow-marine sequences as the building blocks of stratigraphy: insights from numerical modeling: Basin Research, v. 15, p. 287–303.

Storms, J.E.A., Weltje, G.J., van Dijke, J.J., and Kronenberg, S.B., 1999, 2D process–response modeling of shoreface evolution and barrier island behavior on geological time-scales, *in* Lippard, S.J., Næs, A., and Sinding-Larsen, R., eds., Proceedings of the International Association for Mathematical Geology: Trondheim, Norway, p. 563–568.

Storms, J.E.A., Weltje, G.J., van Dijke, J.J., Geel, C.R., and Kronenberg, S.B., 2002, Process–response modeling of wave-dominated coastal systems: simulating evolution and stratigraphy on geological timescales: Journal of Sedimentary Research, v. 72, p. 226–239.

Swift, D.J.P., 1975, Barrier-island genesis: evidence from the central Atlantic Shelf, eastern U.S.A.: Sedimentary Geology, v. 14, p. 1–43.

Swift, D.J.P., Parsons, B.S., Foyle, A., and Oertel, G.F., 2003, Between beds and sequences: stratigraphic organization at intermediate scales in the Quaternary of the Virginia coast, USA: Sedimentology, v. 50, p. 81–111.

Syvitski, J.P.M., and Bahr, D.B., 2001, Numerical Models of Marine Sediment Transport and Deposition: Computers and Geosciences, v. 27, p. 617–753.

Syvitski, J.P., and Hutton, E.W.H., 2001, 2D SEDFLUX 1.0C: An advanced process–response numerical model for the fill of marine sedimentary basins: Computers and Geoscience, v. 27, p. 731–754.

Tamura, T., Masuda, F., Sakai, T., and Fujiwara, O., 2003, Temporal development of prograding beach-shoreface deposits: the Holocene of Kujukuri coastal plain, eastern Japan: Marine Geology, v. 198, p. 191–207.

Taylor, K.G., Gawthorpe, R.L., and Van Wagoner, J.C., 1995, Stratigraphic control on laterally persistent cementation, Book Cliffs, Utah: Geological Society of London, Journal, v. 152, p. 225–228.

Taylor, K.G., Gawthorpe, R.L., Curtis, C.D., Marschall, J.D., and Awwiller, D.N., 2000, Carbonate cementation in a sequence-stratigraphic framework: upper Cretaceous sandstones, Book Cliffs, Utah–Colorado: Journal of Sedimentary Research, v. 70, p. 360–372.

Taylor, S.P., and Sellwood, B.W., 2002, The context of lowstand events in the Kimmeridgian (Late Jurassic) sequence stratigraphic evolution of the Wessex–Weald Basin, southern England: Sedimentary Geology, v. 151, p. 89–106.

Tribovillard, N., Bialkowski, A., Tyson, R.W., Lallier-Verges, E., and Deconinck, J.F., 2001, Organic facies variations in the Late Kimmeridgian of the Boulonnais area (northernmost France): Marine and Petroleum Geology, v. 18, p. 371–389.

Tucker, M.E., and Wright, V.P., 1990. Carbonate Sedimentology: London, Blackwell Scientific Publications, 482 p.

Vail, P.R., Mitchun, R.M., and Thompson, S, III, 1977, Seismic stratigraphy and global changes of sea level, part 5: Chronostratigraphic significance of seismic reflections, *in* Payton, C.E., ed., Seismic Stratigraphy—Applications to Hydrocarbon Exploration: American Association of Petroleum Geologists, Memoir 26, p. 99–116.

Van Wagoner, J.C., Posamentier, N.W., Mitchum, R.M., Vail, P.R., Sarg, J.F., Loutit, T.S., and Hardenbol, J., 1988, An overview of the fundamentals of sequence stratigraphy and key definitions, *in* Wilgus, C.K., Hastings, B.S., Kendall, C.G.St.C., Posamentier, H.W., Ross, C.A., and Van Wagoner, J.C., eds., Sea-level Changes—An Integrated Approach: SEPM, Special Publication 42, p. 39–45.

Van Wagoner, J.C., Mitchum, R.M., Campion, K.M., and Rahmanian, V.D., 1990, Siliclastic sequence stratigraphy in well logs, cores and outcrops: concepts for high resolution correlation of time and facies: American Association of Petroleum Geologists, Methods in Exploration, v. 7, p. 1–55.

Vernik, L., and Nur, A., 1992, Petrophysical classification of siliciclastics for lithology and porosity predictions from seismic velocities: American Association of Petroleum Geologists, Bulletin, v. 76, p. 1295–1309.

Warrlich, G.M.D., Waltham, D.A., and Bosence, D.W.J., 2002, Quantifying the sequence stratigraphy and drowning mechanisms of atolls using a new 3D forward stratigraphic modeling program (CARBONATE 3D): Basin Research, v. 14, p. 379–400.

Wignall, P.B., 1991, Test of the concepts of sequence stratigraphy in the Kimmeridgian (Late Jurassic) of England and northern France: Marine and Petroleum Geology, v. 8, p. 430–441.

Wignall, P.B., and Newton, R., 2001, Black shales on the basin margin: a model based on examples from the Upper Jurassic of the Boulonnais, northern France: Sedimentary Geology, v. 144, p. 335–356.

Wignall, P.B., Sutcliffe, O.E., Clemson, J., and Young, E., 1996, Unusual shoreface sedimentology in the upper Jurassic of the Boulonnais, northern France: Journal of Sedimentary Research, v. 66, p. 577–586.

Williams, C.J., Hesselbo, S.P., Jenkyns, H.C., and Morgans-Bell, H.S., 2001, Quartz silt in mudrocks as a key to sequence stratigraphy (Kimmeridge Clay Formation, Late Jurassic, Wessex basin, U.K.): Terra Nova, v. 13, p. 449–455.

Wilson, J.L., 1975. Carbonate differential in geologic history: Berlin, Springer-Verlag, 471 p.

Ziegler, P.A., 1969, Über Exogyra virgula (Lamellibranchiata, Oberjura): Bericht der Schweizerischen Paläontologischen Gesellschaft, v. 62, p. 685–696.

Received 26 May 2004; accepted 18 April 2005.